HHS Public Access

Author manuscript

Cell Rep. Author manuscript; available in PMC 2022 April 19.

Published in final edited form as:

Cell Rep. 2022 March 15; 38(11): 110512. doi:10.1016/j.celrep.2022.110512.

Coordinated changes in glycosylation regulate the germinal center through CD22

Jhon R. Enterina[1], **Susmita Sarkar**[2], **Laura Streith**[1], **Jaesoo Jung**[2], **Britni M. Arlian**[3], **Sarah J. Meyer**[4], **Hiromu Takematsu**[5], **Changchun Xiao**[6], **Troy A. Baldwin**[1], **Lars Nitschke**[4], **Mark J. Shlomchick**[7], **James C. Paulson**[3], **Matthew S. Macauley**[1,2,8,*]

[1]Department of Medical Microbiology and Immunology, University of Alberta, Edmonton, AB T6G 2E1, Canada

[2]Department of Chemistry, University of Alberta, Edmonton, AB T6G 2G2, Canada

[3]Department of Molecular Medicine, The Scripps Research Institute, La Jolla, CA 92037, USA

[4]Division of Genetics, Department of Biology, University of Erlangen, 91058 Erlangen, Germany

[5]Faculty of Medical Technology, Fujita Health University, Aichi 470-1192, Japan

[6]Department of Immunology and Microbiology, The Scripps Research Institute, La Jolla, CA 92037, USA

[7]Department of Immunology, University of Pittsburgh School of Medicine, Pittsburgh, PA 15261, USA

[8]Lead contact

SUMMARY

Germinal centers (GCs) are essential for antibody affinity maturation. GC B cells have a unique repertoire of cell surface glycans compared with naive B cells, yet functional roles for changes in glycosylation in the GC have yet to be ascribed. Detection of GCs by the antibody GL7 reflects a downregulation in ligands for CD22, an inhibitory co-receptor of the B cell receptor. To test a functional role for downregulation of CD22 ligands in the GC, we generate a mouse model that maintains CD22 ligands on GC B cells. With this model, we demonstrate that glycan remodeling plays a critical role in the maintenance of B cells in the GC. Sustained expression of CD22 ligands induces higher levels of apoptosis in GC B cells, reduces memory B cell and plasma cell output,

*Correspondence: macauley@ualberta.ca.

AUTHOR CONTRIBUTIONS

J.R.E. and M.S.M. designed the experiments, analyzed and interpreted the data, and wrote the manuscript. J.R.E. performed all mouse and *ex vivo* experiments. S.S. assisted with all aspects of the mouse experiments. L.S. carried out experiments with iGC B cells. J.J. prepared mCD22-Fc. B.M.A. and J.C.P. helped develop the $R26^{lsl}$-*Cmah* mice. S.J.M. and L.N. provided bone marrow cells from knockin mice containing ITIM-deficient CD22. C.X. and H.T. provided reagents and expert advice for establishing $R26^{lsl}$-*Cmah* mice. T.A.B. provided $Nur77^{GFP}$ mice and advised on their use/data interpretation.M.J.S. provided the *CD20-ERT2*^{Cre} mice and provided critical advice on the project. All authors have read and approved the manuscript.

SUPPLEMENTAL INFORMATION

Supplemental information can be found online at https://doi.org/10.1016/j.celrep.2022.110512.

DECLARATION OF INTERESTS

The authors declare no competing interests.

and delays affinity maturation of antibodies. These defects are CD22 dependent, demonstrating that downregulation of CD22 ligands on B cells plays a critical function in the GC.

Graphical abstract

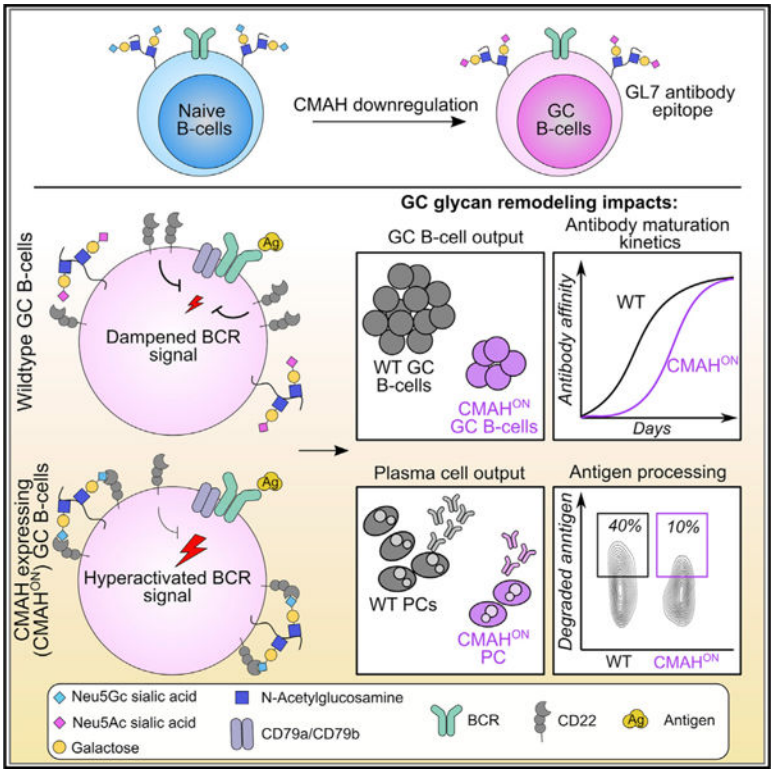

In brief

Changes in glycosylation on GC B cells are hypothesized to affect CD22, an inhibitory BCR co-receptor. Enterina et al. show that altered glycosylation in the GC leads to a CD22-dependent defective GC. Therefore, coordinated changes in glycosylation in the GC play a critical functional role through modulating the function of CD22

INTRODUCTION

Efficient clearance of invading pathogens relies partly on the production of high-affinity antibodies. These antibodies are secreted by plasma cells that emerge from germinal centers (GCs) that transiently form in the secondary lymphoid organs following an infection or vaccination (Berek et al., 1991; Liu et al., 1989). GCs are organized into two functionally distinct compartments: the dark zone (DZ) and light zone (LZ). Within these compartments, GC B cells undergo iterative clonal expansion, diversification of their B cell receptor (BCR) genes through activation-induced cytidine deaminase (AID)-mediated somatic hypermutation (SHM) (Allen et al., 2007; Muramatsu et al., 1999; Victora and Nussenzweig, 2012), and selection for memory B cell and plasma cell differentiation (De Silva and Klein, 2015; Mesin et al., 2016; Victora and Nussenzweig, 2012). Positive

selection relies on the ability of GC B cells to successfully internalize, process and present antigenic epitopes to cognate $CD4^+$ follicular helper T cells (T_{FH}) for positive signals in the form of cytokines and co-stimulatory receptor interactions (Ise et al., 2018; Shulman et al., 2014; Victora and Nussenzweig, 2012). These orchestrated events in the GC ensure a preferential maintenance of B cells with high-affinity BCRs, securing the generation of high-quality antibodies for long-lasting humoral immunity.

Earlier studies revealed that crosslinking of BCR on GC B cells is inefficient in phosphorylating downstream signaling components (Khalil et al., 2012; Luo et al., 2018). Dampening of BCR signaling in GC B cells is mediated by Src homology 2 (SH2) domain-containing protein-tyrosine phosphatase 1 (SHP1) (Alsadeq et al., 2014; Getahun et al., 2016; Sasi et al., 2018). SHP1 negatively regulates BCR activation by binding to phosphorylated immunoreceptor tyrosine-based inhibitory motifs (ITIMs) of BCR inhibitory co-receptors, such as CD22, CD72, PIR-B, Siglec-10/G, FcγRIIb, and FCRL5 (Adachi et al., 2001; Haga et al., 2007; Maeda et al., 1999; Rao et al., 2002; Tsubata, 2018). Effective inhibition of BCR signaling following antigen engagement is essential for a proper GC response, but it is unclear how BCR signal strength is differentially regulated between naive and GC B cells.

In the GC, B cells display remodeling of glycans on cell surface glycoproteins. Several defining events relate to changes in the monosaccharide sialic acid, which caps cell surface *N*- and *O*-linked glycans. These distinct changes are widely used to identify mouse GC B cells. One example is the glycan epitope recognized by the antibody GL7, which emerges from the downregulation of the CMP sialic acid hydroxylase (CMAH) in GC B cells (Naito et al., 2007). GL7 detects glycans terminating in α2–6-linked *N*-acetylneuraminic acid (Neu5Ac) (Macauley et al., 2015; Naito et al., 2007). Downregulation of CMAH prevents the hydroxylation of cytidine monophosphate (CMP) Neu5Ac (CMP-Neu5Ac) and its conversion to CMP-*N*-glycolylneuraminic acid (CMP-Neu5Gc), which is preferentially expressed on naive murine B cells. The switch from Neu5Gc to Neu5Ac on GC B cells has a profound effect on ligands of mouse CD22 (mCD22). Specifically, mCD22 binds to α2–6-linked Neu5Ac-containing glycans 20-fold weaker than α2–6-linked Neu5Gc-containing counterparts (Macauley et al., 2015).

Humans have lost the ability to biosynthesize Neu5Gc because of inactivation of *CMAH* (Chou et al., 1998; Irie et al., 1998). Yet an alternative mechanism downregulates CD22 ligands on human GC B cells, involving a sulfated glycan ligand (Neu5Acα2–6Galβ1–4[6-sulfo]GlcNAc) that is present on naive B cells but not on GC B cells (Kimura et al., 2007; Macauley et al., 2015). Thus, downregulation of CD22 ligands in the GC is an evolutionarily conserved mechanism catering to the related but distinct ligand specificities of mouse and human CD22.

Studies in naive B cells with disrupted CD22-ligand interactions have collectively demonstrated that loss of CD22-ligand interactions leads to blunted B cell responses (Collins et al., 2006; Müller et al., 2013). Mechanistically, CD22-glycan interactions maintain CD22 within nanoclusters, along with CD45 and galectin-9, and away from

the BCR (Cao et al., 2018; Gasparrini et al., 2016). Consequently, ablating CD22-ligand interactions increases CD22-BCR association and dampened BCR signaling.

On the basis of these roles for CD22-glycan interactions on naive B cells, we hypothesized that appearance of the GL7 glycan epitope and concurrent downregulation of CD22 ligands on GC B cells play a crucial role in the GC response by increasing the ability of CD22 to antagonize the BCR signaling. Here, we show that constitutive expression of CMAH impairs the GC response in a CD22-dependent manner. The absence of CD22 or inability to downregulate CD22 ligands leads to higher BCR activation, defective antibody affinity maturation, and increased apoptotic cell death in GC B cells. Collectively, our findings demonstrate that glycan remodeling, through downregulation of CMAH in the GC, is crucial for the maintenance and competitiveness of GC B cells, underscoring GC-specific downregulation of CD22 ligands as a mechanism contributing to rewiring of BCR signaling in the GC.

RESULTS

Constitutive expression of CMAH maintains high-affinity ligands for CD22 on GC B cells

To confirm if appearance of the GL7 epitope on GC B cells occurs through transcriptional downregulation of *Cmah*, we compared the mRNA expression levels of *Cmah* in mouse DZ and LZ GC B cells to follicular B cells using a publicly available dataset (GEO: GSE109125; Yoshida et al., 2019). Follicular B cell levels of *Cmah* transcript are indeed significantly downregulated in both DZ and LZ GC B cells (Figure S1A). To explore the functional role for this switch in sialic acid from Neu5Gc to Neu5Ac as naive B cells differentiate into GC B cells (Figure 1A), we developed a transgenic mouse model to modulate Neu5Gc in a cell type-specific manner. *Cmah* was knocked into the *Rosa26* locus with an upstream loxP-STOP-loxP cassette to enable Cre-dependent expression of CMAH, which we describe as $R26^{lsl}$-*Cmah* mice (Figure 1B). To characterize the effect of constitutive CMAH in B cells, we crossed $R26^{lsl}$-*Cmah* mice with $Mb1^{Cre}$ mice (Hobeika et al., 2006). Immunization of $Mb1^{Cre}\times R26^{lsl}$-*Cmah*, denoted hereafter as $CMAH^{ON}$, mice with chicken ovalbumin (OVA) resulted in GC B cells ($B220^{+}CD19^{+}IgD^{-}CD38^{low}Fas^{+}PNA^{+}$ cells) that do not express the GL7 epitope (Figures 1C and 1D) and maintain Neu5Gc expression at comparable levels to naive B cells ($B220^{+}CD19^{+}IgD^{+}$ cells) (Figures S1B and S1C). Levels of PNA and CD38 staining were indistinguishable between wild-type (WT) and $CMAH^{ON}$ on GC B cells (Figures S1D–S1F). Maintaining CMAH expression in GC B cells also prevented the downregulation of CD22 ligands, as demonstrated by staining with mCD22-Fc (Figures S1G–S1I). In non-immunized mice, the absolute number of major B cell subsets in spleens were slightly lower in $CMAH^{ON}$ compared with their WT counterparts (Figure S1J), but the relative percentage of each subset in total B cells ($CD19^{+}$ live cells) was comparable between WT and $CMAH^{ON}$ splenocytes, except for B1a cells, in which a slight reduction was observed in $CMAH^{ON}$ mice (Figure S1K).

CMAH expression restricts B cell responses in the GC

To test the impact of maintaining CMAH expression in GC B cells, lethally irradiated WT B6 mice were reconstituted with bone marrow (BM) cells from either $R26^{lsl}$-*Cmah* (as WT

control) or CMAH^{ON} mice to generate chimera mice. Reconstituted mice were immunized with liposomes displaying OVA antigen (Figure 1E). Flow cytometric analysis revealed that the total number of GC B cells in immunized CMAH^{ON} mice is comparable to their WT counterparts on day 7 post-immunization (PI) (Figures 1F–1H). However, on days 14 and 21 PI, we observed a significant reduction in the number of GC B cells from immunized CMAH^{ON} mice (Figures 1G and 1H). Immunofluorescence analysis of spleens, collected 14 days PI, identified a decrease in the size of GC clusters (IgD^{-}PNA^{+}) in CMAH^{ON} mice compared with WT mice, validating the phenotype we observed using flow cytometry (Figures 1I–1K). Concurrently, we assessed the generation of OVA-specific GC B cells PI. We also found normal levels of OVA^{+} GC B cells between WT and CMAH^{ON} on day 7 PI, but at later time points, CMAH^{ON} mice had fewer OVA^{+} GC B cells than their WT counterparts (Figures 1L–1N). Within a mixed BM chimera, constitutive expression of CMAH in the B cells led to a competitive disadvantage over WT B cells in the GC on the basis of the higher percentage of WT B cells in the GC (both total and OVA^{+}) compartment than in the naive B cell pool. This phenotype was already noticeable at 7 days PI (Figures S2A–S2C).

Given that CMAH^{ON} mice constitutively express CMAH in B cells starting early in B cell development, we aimed to test if this is a GC-specific phenotype by crossing *R26^{lsl}-Cmah* mice with *Aicda^{Cre}* mice to induce Cre expression 2–3 days PI (Robbiani et al., 2008). Chimera mice were generated by transplanting *Aicda^{Cre}* (WT control) and *Aicda^{Cre}*×*R26^{lsl}-Cmah* BM cells. After immunization, we assessed the percentage of *Aicda^{Cre}* in the GC B cell compartment in comparison with their counterparts in the naive B cell pool. We found that OVA^{+} WT GC B cells were outcompeting *Aicda^{Cre}*×*R26^{lsl}-Cmah* GC B cells 2 weeks PI (Figure S2D). Similar findings were made by microscopy when examining immunized spleens from WT and *Aicda^{Cre}*×*R26^{lsl}-Cmah* mice (Figures S2E–S2G). Expression of CMAH was also temporally induced in the B cell lineage by crossing human *CD20-ERT2^{Cre}* and *R26^{lsl}-Cmah* mice and administering tamoxifen on days 8 and 9 PI (Alsadeq et al., 2014), and a competitive disadvantage of *CD20-ERT2^{Cre}* over *CD20-ERT2^{Cre}*×*R26^{lsl}-Cmah* was also observed in the GC compartment (Figures S2H and S2I). These findings demonstrate that downregulation of CMAH expression is essential for the maintenance of B cells in the GC.

Impaired GC response in CMAH transgenic B cells is dependent on CD22

The function of mCD22 is regulated by its *cis* ligands, and the preferred glycan ligands of CD22 require CMAH (Macauley et al., 2015). Therefore, we tested whether sustained expression of CMAH in GC B cells negatively affects the GC response through CD22 by crossing CD22^{KO} mice and CMAH^{ON} mice. Mixed BM chimeras were set up using cells from CD22^{KO} and CD22^{KO}×CMAH^{ON} donor mice. Following immunization, the previously observed competitive disadvantage in CMAH^{ON} GC B cells was no longer observed (Figure 2A). We also tested this in an adoptive transfer model, using hen egg lysozyme (HEL)-specific B cells on a CD22^{KO} and CD22^{KO}×CMAH^{ON} background and tracked the formation of HEL^{+} GC B cells in competition (Figure 2B). After immunization with HEL-displaying liposomes, the ratio of adoptively transferred cells was comparable with their unimmunized counterparts (Figure 2C). In contrast, immunization of mice

adoptively transferred with HEL-specific B cells on a WT and CMAH^{ON} background displayed a clear competitive disadvantage for CMAH^{ON} GC B cells (Figure 2D). Together, these *in vivo* experiments support the hypothesis that the critical role of programmed CMAH downregulation in the maintenance of GC B cell response is dependent on CD22.

CD22 is critical for B cell competitiveness in the GC

To directly test if CD22 is critical for GC B cell responses, we generated mixed chimera mice transplanted with WT and *Cd22*^{KO} BM cells and then immunized them with OVA-displaying liposomes. OVA^{+} WT GC B cells significantly outcompeted OVA^{+} CD22^{KO} GC B cells even starting on day 7 PI (Figures 2E–2H). Within mixed bone marrow chimeras between WT and CD22^{KO} or WT and CMAH^{ON}, trends for WT having a competitive advantage were similar in the spleen, inguinal lymph node (LN), and axillary LN (Figures S3A–S3C). To assess whether this defective GC B cell response observed with CD22^{KO} B cells is B cell specific, we generated floxed CD22 (*Cd22*$^{f/f}$) mice and crossed them first with *Mb1*^{Cre} mice. Following immunization of mixed chimera mice transplanted with WT and *Mb1*^{Cre}×*Cd22*$^{f/f}$ BM cells, antigen-specific WT B cells outcompeted the *Mb1*^{Cre}×*Cd22*$^{f/f}$ B cells in the GC, validating that the GC defect observed in CD22^{KO} mice is B cell intrinsic (Figure 2I). We next crossed *Cd22*$^{f/f}$ mice with *Aicda*^{Cre} mice. Tracking antigen-specific GC B cell formation in immunized mixed chimera mice reconstituted with *Aicda*^{Cre} (WT control) and *Aicda*^{Cre}×*Cd22*$^{f/f}$ BM cells, we observed a competitive disadvantage for *Aicda*^{Cre}×*Cd22*$^{f/f}$ GC B cells on days 14 and 21 PI (Figure 2J). To assess whether the impaired GC response in CD22^{KO} B cells is dependent on its ITIMs, we tracked the antigen-specific GC B cell response of WT and CD22$^{Y-2,5,6-F}$ B cells, which have knockin mutations in three of its key cytoplasmic ITIMs (Müller et al., 2013). Following immunization, we identified that loss of functional ITIMs on CD22 resulted in poor GC B cell response, recapitulating a similar phenotype seen in CD22^{KO} GC B cells (Figure 2K). These results strongly suggest that regulation of signaling by CD22 is required for the maintenance of GC B cells.

Loss of CD22 impairs interzonal distribution of GC B cells

Repeated migration of GC B cells between the DZ and LZ ensures the maintenance and selection of clones with high-affinity BCRs. To test whether CMAH expression or loss of CD22 affects DZ/LZ distribution in the GC, we probed DZ and LZ GC B cells using flow cytometry (Figure S3D). After immunization, we found a normal distribution of CMAH^{ON} GC B cells in the DZ and LZ compartments (Figure S3E). However, CD22^{KO} GC B cells displayed fewer LZ GC B cells than WT GC B cells (Figure S3F). Consistent with the result by flow cytometry, immunofluorescence staining of spleens showed that the percentage of GC B cells in the LZ (IgD^{-}PNA^{+}CD21/35^{+}), compared with the total GC, was significantly lower in CD22^{KO} mice compared with WT and CMAH^{ON} mice (Figures S3G and S3H).

Ablation of CD22 and constitutive expression of CMAH impairs antibody affinity maturation

To evaluate whether the defective GC B cell response observed in CD22^{KO} and CMAH transgenic models results in defective humoral immunity, we immunized WT, CD22^{KO}, and CMAH^{ON} mice with liposomes that display OVA conjugated with NP-hapten (Figure

3A). Antibody affinity maturation was determined by monitoring high-affinity αNP IgG1 and total αNP IgG1 antibody, using NP_2-BSA and NP_{23}-BSA, respectively, by ELISA at different time points PI. The NP_2/NP_{23} ratio of the half maximal inhibitory concentration (IC_{50}) values in the ELISAs were used to estimate antibody affinity maturation, with a higher NP_2/NP_{23} ratio being indicative of better antibody affinity maturation. We found that deficiency in CD22 impaired the maturation of αNP antibodies and were not able to recover even at a later time point (day 42) PI. $CMAH^{ON}$ mice also displayed a significant, yet modest, reduction in antibody affinity maturation at earlier time points PI, but this difference compared with WT mice was no longer apparent by day 42 (Figure 3B). To investigate whether this defective production of high-affinity antibodies in $CD22^{KO}$ mice is due to diminished SHM, NP-specific GC B cells ($B220^+CD19^+IgD^-GL7^+NP_{20}^+$ cells) were isolated using fluorescence-activated cell sorting (FACS) from WT and $CD22^{KO}$ mice, at 21 days PI with NP-OVA-displaying liposomes. The $V_H186.2$ region was sequenced and found to have a similar mutation rate between WT and $CD22^{KO}$ (Figures 3C–3E). Additionally, we also observed a comparable number of clones between WT (n = 15 of 33) and $CD22^{KO}$ (n = 17 of 32) with the affinity-enhancing mutations W33L and K59R (Furukawa et al., 1999) (Figure 3F).

To assess whether CD22 and its *cis* ligands control the maintenance of GC B cell clones with high-affinity BCRs, we quantified the number of high-affinity NP^+ and total NP^+ GC B cells in WT, $CD22^{KO}$, and $CMAH^{ON}$ mice, immunized with NP-OVA-displaying liposomes, using flow cytometry at day 14 PI. We found that the absolute numbers of both high-affinity NP^+ and total NP^+ GC B cells, identified with NP_4-APC and NP_{20}-APC, respectively (Figure 3G), were significantly lower in $CD22^{KO}$ and $CMAH^{ON}$ mice compared with WT (Figures 3H and 3I). Likewise, the ratio of high-affinity over total NP^+ GC B cells was also substantially reduced in $CD22^{KO}$ and $CMAH^{ON}$ mice (Figure 3J). These findings demonstrate that CD22 and loss of its *cis* ligands on GC B cells are pivotal for the maintenance of B cell clones with high-affinity BCRs.

Attenuated memory B cell and plasma cell output in $CD22^{KO}$ and $CMAH^{ON}$ mice

Given that both $CMAH^{ON}$ and $CD22^{KO}$ mice show reduced numbers of antigen-specific GC B cells following immunization, we investigated whether this finding correlates with decreased memory B cell and plasma cell output as well. To test this, we quantified the number of NP^+ memory B cells ($B220^+CD19^+IgD^-CD38^{high}PNA^-NP_{20}^+$ cells) and plasma cells ($CD138^{high}CD19^-NP_{20}^+$ cells) using flow cytometry (Figure S4A). We found that spleens of $CMAH^{ON}$ and $CD22^{KO}$ mice, after day 14 PI with NP-OVA-displaying liposomes, displayed remarkably lower numbers of both memory B cells and plasma cells than their WT counterparts (Figures S4B–S4G). These data indicate that decreased antibody responses observed in $CMAH^{ON}$ and $CD22^{KO}$ mice are likely due to reduced plasma cells emerging from the GC.

Transcriptome analysis reveals a crucial role of CD22 in maintaining B cell fitness in the GC

To determine the putative mechanisms responsible for the defective GC response in $CD22^{KO}$ B cells, we analyzed the impact of CD22 deficiency on the transcriptome profile of GC B

cells. To achieve this, we collected spleens from WT and $CD22^{KO}$ mice at day 14 PI where the defective GC phenotype was observed. The DZ ($B220^{+}CD19^{+}IgD^{-}GL7^{+}CXCR4^{high}$-$CD86^{low}$) and LZ ($B220^{+}CD19^{+}IgD^{-}GL7^{+}CXCR4^{low}CD86^{high}$) GC B cells from splenocytes were sorted using FACS, and RNA was isolated and processed for next-generation sequencing (Figures S5A–S5C). We found numerous differentially expressed genes (DEGs) that are either upregulated or downregulated in $CD22^{KO}$ GC B cells (Figures 4A–4C). Interestingly, we observed more DEGs in the LZ than in the DZ GC compartment. These include genes encoding for GIMAP GTPase family, mitochondrial enzymes, cell cycle regulatory proteins, GC-relevant transcription factors, and B cell activation signaling proteins (Tables S1 and S2). To interrogate the distinct biological processes and pathways disrupted in the GC because of the loss of CD22, a gene enrichment analysis was performed using EnrichR with DEGs with p values < 0.05. We found that both DZ and LZ $CD22^{KO}$ GC B cells displayed defective oxidative phosphorylation, cell cycle progression, and cholesterol biosynthesis. On the other hand, upregulated genes in $CD22^{KO}$ GC B cells converged on pathways for B cell activation, Toll-like receptor signaling, and apoptosis (Figures 4D and 4E). Interestingly, an enrichment for Myc target genes was also evident within both DZ and LZ populations of the WT versus $CD22^{KO}$ GC B cells (Figures S5D and S5E). Thus, transcriptome analysis uncovers that expression of CD22 controls B cell activation and other processes relevant for B cell competitiveness in the GC.

$CD22^{KO}$ and $CMAH^{ON}$ GC B cells display hyperactivated BCR signaling

Previous studies demonstrated that GC B cells display a highly inhibited phenotype compared with non-GC B cell populations (Alsadeq et al., 2014; Getahun et al., 2016). To interrogate whether this phenotype is partly controlled by CD22, we used an *in vivo* reporter for BCR activation, Nur77-GFP (Mueller et al., 2015), to probe the degree of activation between WT and $CD22^{KO}$ GC B cells. We immunized $Nur77^{GFP}$ (WT control) and $CD22^{KO}3Nur77^{GFP}$ mice with OVA-displaying liposomes (Figure 5A). After immunization, we found that $CD22^{KO}$ mice produced more GFP^{+} DZ (Figures 5B–5D) and LZ (Figures 5E–5G) GC B cells than WT. GFP expression in $CD22^{KO}$ GC B cells is also evidently higher than WT, suggesting increased activity of the Nur77 promoter in GC B cells. Consistent with this observation, transcript analysis confirmed increased expression of *Nr4a1*, which encodes for Nur77 (Figure 5H). As the $Nur77^{GFP}$ reporter mouse could not be used with $CMAH^{ON}$, because of bicistronic expression of GFP in the $CMAH^{ON}$ mice, we examined the protein levels of Nur77 by intracellular flow cytometry on GC B cells from within mixed bone marrow chimeras (Figure S6A). Both $CMAH^{ON}$ and $CD22^{KO}$ GC B cells had significantly higher levels of Nur77 compared with their WT counterparts (Figures S6B and S6C).

We next examined changes in intracellular Ca^{2+} mobilization in $CMAH^{ON}$ or $CD22^{KO}$ GC B cells in competition with WT GC B cells, following BCR crosslinking (Figure 5I). Following stimulation with goat $F(ab')_2$ αmouse Igκ, we found that $CMAH^{ON}$ GC B cells ($B220^{+}CD38^{low}PNA^{+}$) displayed approximately 2-fold higher Ca^{2+} mobilization compared with their WT counterparts (Figures 5J and 5K). In the same tube, non-GC B cells ($B220^{+}CD38^{+}PNA^{-}$) showed no difference between the two genotypes (Figure 5L). Similarly, $CD22^{KO}$ GC B cells exhibited increased Ca^{2+} flux compared with WT GC B

cells, which appeared to be even more noticeably enhanced than in the naive compartment (Figures 5M–5O). We also isolated B cells and examined phosphorylation of BCR signaling components Syk and Akt (both S474 and T308) at different time points after aBCR stimulation (Figure S6D). $CMAH^{ON}$ GC B cells displayed modest hyperactivation of pAkt at S473 (Figures S6E–S6G), while $CD22^{KO}$ GC B cells showed hyperactivation of all three targets (Figures S6H–S6J). These findings indicate that CD22 and natural downregulation of its ligands on GC B cells control the activation of BCR-mediated signaling following antigen engagement.

GC B cells from $CD22^{KO}$ and $CMAH^{ON}$ mice display reduced MHC-II expression and defective antigen processing

To investigate whether CD22 plays a role in the ability of GC B cells to interact with T_{FH} cells, we first assessed whether surface expression of MHC-II is regulated by CD22 or its *cis* ligands. Expression of MHC-II in $CMAH^{ON}$ and $CD22^{KO}$ GC B cells on day 7 PI was comparable with their WT counterparts, but on day 14 PI, both $CMAH^{ON}$ and $CD22^{KO}$ expressed less surface MHC-II (Figures 6A and 6B). Interestingly, the transcript levels of the gene encoding for MHC-II (*H2-Ab1*) were comparable between WT and $CD22^{KO}$ GC B cells, isolated from mice after day 14 PI (Tables S1 and S2). As MHC-II protein levels are regulated post-translationally (De Gassart et al., 2008; Liu et al., 2016), it is noteworthy that levels of *Marchf1* and *Cd83* were not altered in $CD22^{KO}$ GC B cells in a direction that would result in decreased MHC-II levels. We next checked if this phenotype is due to defective antigen internalization or processing by interrogating antigen internalization, through assessing the levels of surface BCR following BCR crosslinking with soluble antigen. Both $CMAH^{ON}$ and $CD22^{KO}$ GC B cells displayed similar rates of BCR internalization compared with WT GC B cells, indicating that CD22 and alterations to its *cis* ligands are dispensable for proper internalization of antigen-BCR complex (Figures 6C–6F). Additionally, we explored whether processing of endocytosed antigen is defective in $CMAH^{ON}$ or $CD22^{KO}$ GC B cells. In order to do this, an *ex vivo* antigen degradation assay was used, which relies on a double-stranded DNA (dsDNA)-based sensor that is fluorescently quenched in its undegraded state (Nowosad et al., 2016). Upon antigen degradation in the lysosome, the dsDNA sensor is degraded, leading to an increase in Atto647 fluorescence. Using this method, we found that both $CMAH^{ON}$ and $CD22^{KO}$ GC B cells showed significantly lower antigen degradation than their WT counterpart after BCR stimulation (Figures 6G–6I). Furthermore, reduced antigen degradation in $CMAH^{ON}$ GC B cells is dependent on the expression of CD22 on these cells (Figure 6J). Control experiments conducted with a sensor lacking the quencher and carried out on ice enabled an assessment of cell binding (Figure S7). Collectively, these findings suggest that loss of CD22 expression or the inability to downregulate CD22 ligands in GC B cells leads to decrease cell surface levels of MHC-II, which may be due partly to impaired antigen processing.

Antigen delivery via αDEC205-OVA rescues defective GC responses in $CD22^{KO}$ B cells

The defective antigen processing and MHC-II expression on $CD22^{KO}$ or $CMAH^{ON}$ GC B cells suggests that B-T cell interactions may be compromised. To override defective antigen presentation, we used a previously established approach to deliver antigen to GC B cells through a non-BCR-dependent pathway (Pasqual et al., 2015). Antigen delivered

through the DEC205 receptor is known to increase pMHC-II presentation and $CD4^+$ T_{FH} interactions. To do so, mixed chimera mice reconstituted with $DEC205^{KO}$ and $CD22^{KO}$ BM cells were injected with αDEC205-OVA or PBS 11 days after immunization with OVA-displaying liposomes (Figure 6K). Three days later (day 14), we found that administration of αDEC205-OVA, but not PBS, restored the levels of antigen-specific $CD22^{KO}$ GC B cells to a comparable ratio of $CD22^{KO}$ B cells in the naive population (Figure 6L). A similar rescue was observed in a mixed chimera of $DEC205^{KO}$ and WT cells using the same experimental setup (Figure 6M), although it is difficult to directly assess these last two experiments for the purpose of determining if there is a full rescue in the $CD22^{KO}$ GC B cells upon αDEC205-OVA administration.

Pathway analysis of LZ WT and LZ $CD22^{KO}$ GC B cell transcriptome profile revealed enrichment of gene signatures for Myc targets and mTORC1 signaling in WT (Figures 4F, S8A, and S8B). Given that these pathways are readouts for productive B-T cell interactions in the GC (Calado et al., 2012; Dominguez-Sola et al., 2012; Ersching et al., 2017), we tested whether the rescue of $CD22^{KO}$ GC B cells after αDEC205-OVA treatment is due to upregulation of Myc and mTORC1 pathways. To address this, we examined the levels of Myc and phosphorylated ribosomal S6 (p-S6) proteins following administration of αDEC205-OVA. Here, we injected αDEC205-OVA intravenously in WT and $CD22^{KO}$ mice on day 13 PI with OVA-displaying liposomes. Myc and pS6 expression in GC B cells were evaluated approximately 15 h after delivery of αDEC205-OVA. Although we could not observe a statistically significant increase in Myc levels on total GC B cells (Figures S8C–S8E), gating on LZ GC B cells revealed an increase in the percentage of Myc^{high} cells in the WT but not the $CD22^{KO}$ population (Figures S8F–S8H). For p-S6, both WT and $CD22^{KO}$ GC B cells showed an increase in response to delivery of αDEC205-OVA (Figures S8I–S8K). These results demonstrate that delivering excess antigen to $CD22^{KO}$ GC B cells can rescue defects in either antigen processing or B-T cell interactions in $CD22^{KO}$ GC B cells.

CD22 is critical for the proliferation and survival of B cells in the GC

To test whether CD22 is important in GC B cell proliferation, we injected immunized mixed chimeras transplanted with an equal ratio of WT and *Cd22*^{KO} BM cells with BrdU, which labels proliferating cells. Using flow cytometry, we identified a substantially lower number of $BrdU^+$ $CD22^{KO}$ GC B cells than their WT counterparts (Figures 7A and 7B). However, we did not observe this difference in $CMAH^{ON}$ GC B cells (Figures 7C and 7D). We further investigated this difference in proliferation between WT and $CD22^{KO}$ by examining whether it correlates with impaired cell cycle progression, by determining the cell cycle phases using BrdU and 7-AAD (Figure 7E). We found a larger number of $CD22^{KO}$ GC B cells in the G0-G1 phase ($BrdU^-$7-AAD^{low}) and a smaller number in the S phase ($BrdU^+$) and G2-M ($BrdU^-$7-AAD^{high}) phases compared with WT GC B cells (Figure 7F). These data are consistent with a defective cell cycle transition in $CD22^{KO}$ B cells observed from the transcriptome analysis above. We also observed a modestly higher number of $CMAH^{ON}$ GC B cells in both the S and G2-M phases than their WT counterparts (Figure 7G). These findings indicate that CD22 is required for effective expansion of B cells in the GC.

To investigate whether CD22 or loss of its ligands is necessary for survival of B cells in the GC, we stained splenocytes from immunized WT, $CMAH^{ON}$, and $CD22^{KO}$ mice, at day 14 PI, with αAct-Casp3 antibody, which is an established marker for cells undergoing apoptotic cell death (Porter and Jänicke, 1999). We found a larger number of $CD22^{KO}$ B cells undergoing apoptosis in both the DZ and LZ compartments than WT (Figure 7H). On the other hand, in $CMAH^{ON}$ B cells, only the B cells in the LZ compartment displayed heightened apoptosis compared with WT.

We were interested in understanding whether this increased apoptosis in CD22 is related to hyperactivation of the BCR following stimulation. To examine this, we co-cultured WT, $CMAH^{ON}$, or $CD22^{KO}$ naive B cells with an engineered mouse fibroblast expressing CD40L and BAFF (i.e., CD40LB feeder line) (Nojima et al., 2011) in the presence of mIL4 to induce the differentiation of naive ($B220^{+}CD19^{+}IgD^{+}$) B cells into GC-like ($B220^{+}CD19^{+}IgD^{-}PNA^{+}Fas^{+}$) cells, denoted as iGC. We continued culturing these iGC cells either with mIL4 or mIL4 and αmouse Igk (Figure S9A). Following culture, we found that iGC cells that lack CD22 produced more apoptotic cells in the presence of BCR stimulant (Figures S9B and S9C). In contrast, WT iGC showed no difference in the levels of apoptotic cells in either culture conditions. On the other hand, $CMAH^{ON}$ iGC B cells displayed a slight but significant reduction in the apoptotic cells than their WT counterparts (Figures S9B and S9C). This *in vitro* experiment supports the idea that effective dampening of B cell activation by CD22 is crucial for the survival of B cells in the GC.

We next tested whether this enhanced apoptosis in $CD22^{KO}$ iGC *in vitro* leads to reduction in induced plasmablast (iPB; $CD138^{high}CD19^{+}$ cells) formation. To do this, a 1:1 ratio of WT and $CD22^{KO}$ or $CMAH^{ON}$ naive B cells were co-cultured onto the CD40LB feeder line. Following establishment of iGC cells in culture, we continued co-culturing cells onto CD40LB cells in the presence of either mIL21 or mIL21 and αmouse Igκ. Supplementation of mIL21 induces the differentiation of iGC into plasmablasts *in vitro* (Figures S9D–S9H) (Nojima et al., 2011). After day 8 of co-culture, we found that addition of BCR stimulant in culture resulted in more WT iGC cells differentiating into iPB cells compared with the ratio of differentiated WT iPBs in culture supplemented with mIL21 alone (Figures S9I and S9J). These findings suggests that enhanced BCR signaling, mediated by loss of CD22 or constitutive expression of CMAH, is detrimental to the differentiation of GC B cells into plasmablasts *in vitro*.

Overall, our results build on the knowledge of CD22-glycan interactions in controlling B cell responses. On naive B cells, CD22 is maintained away from the BCR in nanoclusters with itself and other partners. On GC B cells, glycan remodeling is expected to increase association of CD22 with the BCR, thereby increasing its ability to antagonize BCR signaling compared with naive B cells. Given that CD22 has been implicated in Myc and mTORC signaling pathways on GC B cells, we hypothesize that unmasking of CD22 in the GC through CMAH downregulation enhances *trans* interaction with other key cell players in the GC response, such as T_{FH} cells (Figure 7I). Preventing glycan remodeling on GC B cells in the $CMAH^{ON}$ model or loss of CD22 increases BCR signaling, leading to impaired GC B cell responses.

DISCUSSION

Glycans are complex carbohydrate structures covalently bound to protein and lipid carriers. The abundance and composition of glycans have been correlated to phenotype and differentiation of immune cells (Comelli et al., 2006; Dias et al., 2018; Marth and Grewal, 2008). Glycan remodeling has become an increasingly important biological mechanism that cells use to rapidly alter signaling (Johswich et al., 2014; Parker and Kohler, 2010; Tu et al., 2017). In this study, we probed the physiological role of glycan remodeling on GC B cells, which results in the generation of the GL7 epitope, α2–6-linked Neu5Ac, and downregulation of the preferred glycan ligands of CD22 on GC B cells, which is α2–6-linked Neu5Gc (Macauley et al., 2015). This was carried out by studying $CMAH^{ON}$ mice, which enabled CMAH expression to be maintained using a Cre recombinase in the B cell lineage. Our *in vivo* experiments identified that this specific change in glycosylation is crucial for the maintenance of antigen-specific GC B cells, generation of plasma cells and memory B cells, and affinity maturation of antibodies. The defective GC in mice with B cells constitutively expressing α2–6-linked Neu5Gc is dependent on CD22, highlighting that coordinated downregulation of CD22 ligands acts to fine-tune the BCR signal in the GC by modulating the CD22. Moreover, deletion of CD22 on B cells also showed defective GC and antibody responses despite normal SHM and ability to generate affinity-enhancing mutations in the immunoglobulin gene. We hypothesize that downregulation of CD22-glycan ligands on glycoproteins, such as CD45 and CD22 (Bakker et al., 2002; Ramya et al., 2010; Sgroi et al., 1995), disrupts the formation and maintenance of CD22 nanoclusters on GC B cells, leading to a more rapid dissemination of CD22 molecules and attenuation of BCR signaling.

It was not entirely surprising that the GC defects we observed in $CD22^{KO}$ B cells are not fully recapitulated in $CMAH^{ON}$ B cells. Indeed, $CMAH^{ON}$ GC B cells displayed normal proliferation and modest, yet significant, defects in antibody affinity maturation, Ca^{2+} mobilization, and apoptosis compared with $CD22^{KO}$ GC B cells. Given that the presence of high-affinity ligands for CD22 does not completely inhibit CD22 mobilization, as previously described (Collins et al., 2004), we believe that constitutive expression of high-affinity ligands on $CMAH^{ON}$ GC B cells only partially prevents CD22 interaction with the BCR, resulting in less profound defects than the $CD22^{KO}$ GC B cells. Nevertheless, our findings support the model in which dampened BCR signaling favors selection and maintenance of GC B cell clones with high-affinity BCRs.

A previous study also described a role for CD22 in the GC reaction (Chappell et al., 2017). The authors found comparable levels of GC differentiation and normal antibody responses between WT and $CD22^{KO}$ B cells, along with reduced antigen-specific memory B cells and plasma cells from the $CD22^{KO}$ B cells. Differences in study design likely account for this difference. In our studies, we found that in the absence of competition with WT GC B cells, a GC defect in $CD22^{KO}$ mice was observed only beginning at day 14 PI, while Chappell et al. investigated GC B cell responses only up until day 7 PI. Moreover, Chappell et al. used adoptively transferred high-affinity B cell clones, while we primarily examined the formation of GCs from endogenous antigen-specific B cells.

A recent study by Luo et al. (Luo et al., 2019) explored the molecular mechanism downstream of the BCR complex that may be altered, leading to attenuated BCR signaling in GC B cells. The authors identified that GC B cells have an altered AKT-mediated signaling network, which was pinpointed to differential AKT T308 and S473 phosphorylation. Our study demonstrated another intrinsic remodeling that occurs in GC B cells that may be linked to reduced BCR signal activation. By tracking Nur77 promoter activity through GFP reporter expression and *ex vivo* intracellular Ca^{2+} mobilization following BCR crosslinking, we found that CD22 and loss of its *cis* ligands, in part, maintains a hypoactivated phenotype in GC B cells. Furthermore, we demonstrated that enhanced BCR signaling in GC B cells lacking CD22 or constitutively expressing the preferred CD22 ligands is linked to increased GC B cell apoptosis and reduced plasma cell output. Several factors may be in play to promote activation-induced cell death (AICD) in GC B cells. A study by Akkaya et al. (Akkaya et al., 2018) demonstrated that BCR activation increased oxidative phosphorylation and glycolytic activities in B cells. However, prolonged BCR signaling, resulting in intracellular reactive oxygen species (ROS) and Ca^{2+} accumulation, impaired mitochondrial function, leading to AICD. Strikingly, the presence of a second signal coming from cognate T cells was able to rescue both the mitochondrial dysfunction and AICD. Findings from our transcriptome analysis revealed that besides controlling the BCR activation, CD22 is also essential for proper metabolic function and expression of many mitochondrial enzymes. Thus, we speculate that enhanced BCR signal in $CD22^{KO}$ and $CMAH^{ON}$ GC B cells may have induced a defective mitochondrial function; and for GC B cells with low- to moderate-affinity BCRs, which are believed to have a competitive disadvantage for GC T_{FH} help, this dysfunction may have resulted in their eventual demise.

Strength of GC B cell interaction with their cognate T_{FH} cells dictates the differentiation of GC B cells into plasma cells (Ise et al., 2018; Turner et al., 2018). Previously, it was suggested that downregulation of ligands for CD22 on B cells increased B-T conjugation through enhancement of *trans* interaction of CD22 with its ligands on T cells (Naito-Matsui et al., 2014). The downregulation Myc and mTORC signatures in our transcriptional analysis are suggestive of impaired B-T cell interactions in $CD22^{KO}$ and $CMAH^{ON}$ GC B cells. However, in addition to CD22 on GC B cells being better able to interact with *trans* ligands, we also uncovered two other factors that could influence B-T cell interactions: (1) reduced expression of MHC-II in $CD22^{KO}$ and $CMAH^{ON}$ GC B cells and (2) defective antigen processing. Forcing GC B-T_{FH} interaction *in vivo*, by administration of αDEC-antigen following the establishment of the GC, rescued the disadvantage of not having CD22. This suggests that by-passing defects in any (or all three) of these potential roles for CD22 rescues $CD22^{KO}$ GC B cells. This warrants further investigations, such as examining more directly the impact in the GC T_{FH} and interrogating whether CD22 is involved in CD40L surface mobilization or proper secretion of GC-relevant cytokines. Regardless, it appears likely that a role for CD22 and changes in glycosylation go beyond a role in regulating BCR signaling, which may be why $CD22^{KO}$ GC B cells have a more dramatic phenotype than $CMAH^{ON}$ GC B cells.

Maintenance of positively selected GC B cells depends mainly on its ability to cycle between the LZ and DZ and sustaining a robust and fast proliferation while in the DZ.

Following GC T_{FH} interaction, GC B cells activate the mechanistic target of rapamycin complex 1 (mTORC1) and Myc transcription factor to support cell growth and cell cycle progression of B cells in the GC (Calado et al., 2012; Dominguez-Sola et al., 2012; Ersching et al., 2017). Our transcriptome analysis uncovered that CD22 is required by GC B cells to properly regulate the cell cycle machinery, which includes E2F regulated genes, Aurora and PLK1 kinase signaling, and cell cycle checkpoint genes. Using *in vivo* BrdU labeling, we found that $CD22^{KO}$ GC B cells proliferate less and display impaired cell cycle progression, validating the transcriptome finding. Although loss of CD22 has been correlated with hyperproliferation in naive B cells through the activation of the PI3K-AKT pathway, it is possible that constrained BCR signaling, partly controlled by CD22, is responsible for maintaining a rewired AKT activity in the GC. Interestingly, AKT kinase is rewired in the GC B cells to specifically target proteins relevant to cell cycle progression, such as E2F targets, G2/M checkpoints, and Myc targets (Luo et al., 2019). Thus, we can speculate that enhanced BCR signaling through CD22 deletion may lead to altered AKT activity in the GC and loss of substrate selectivity. Another explanation for the reduced proliferation of $CD22^{KO}$ GC B cells can be derived from our transcriptome data. DZ $CD22^{KO}$ GC B cells displayed an impaired cholesterol biosynthesis pathway. Cholesterol is a critical component of the cell membrane and the ability of GC B cells to synthesize cholesterol *de novo* may have structural and signaling benefits, especially in the DZ compartment where B cells induce cellular growth and division (Bléry et al., 2006; Reboldi and Dang, 2018; Singh et al., 2013).

In summary, our findings describe a functional role for the emergence of the glycan epitope for the GL7 antibody. We define that appearance of the GL7 epitope is not merely a defining marker of GC B cells but represents a change in CD22 ligands that plays an important role in fine-tuning BCR signaling within the GC B cells. It is noteworthy that another paper was published during the review of this paper, which supports some of the conclusions in our studies on the role of CD22 in the GC (Meyer et al., 2021). We conclude that loss of CD22 ligands is crucial for the maintenance and selection of GC B cells, as well as affinity maturation antibodies by fine-tuning inhibitory function of CD22 on GC B cells.

Limitations of the study

As Siglecs participate in both *cis* and *trans* interactions, altering CD22-ligand interactions in the GC has the potential to affect both types of interactions. The models used herein make it a challenge to fully disentangle the contributions of abrogated *cis* and *trans* interactions.

STAR★METHODS

RESOURCE AVAILABILITY

Lead contact—Further information and requests for resources and reagents should be directed to and will be fulfilled upon reasonable request by the lead contact, Matthew Macauley (macauley@ualberta.ca).

Materials availability—All unique reagents generated in this study are available from the lead contact without restriction.

Data and code availability

- Next generation sequencing data are deposited in the Gene Expression Omnibus (GEO) database under the accession number GSE196206.
- This paper does not report original code.
- Any additional information required to reanalyze the data reported in this paper is available from the lead contact upon request.

EXPERIMENTAL MODEL AND SUBJECT DETAILS

Mouse strains and frozen bone marrow cells—All mice used in this study were on a C57BL/6J genetic background. C57BL/6J (stock no.:000664), B6-CD45.1 (stock no.:002014), *Mb1*^{Cre} (stock no.:020505), and *Aicda*^{Cre} (stock no.:007770) mice were acquired from Jackson Laboratory. Hy10 mice were a gift from Dr. Jason Cyster (UC San Francisco, USA). Frozen bone marrow cells from *Cd205*^{KO} mice were provided to us by Dr. Gabriel Victora (Rockefeller University, USA). Bone marrow cells were tested for mouse pathogens (Charles River) prior to use.

Rosa26^{lsl}*-Cmah* mice were generated following a previously described protocol (Bednar et al., 2017; Bhattacherjee et al., 2021; Duan et al., 2019). To confirm the genotype of *Rosa26*^{lsl}*-Cmah* mice, PCR was performed using extracted DNA from ear notch samples. The WT Rosa26 locus was identified using 5′-GGAGCGGGAGAAATGGATATG-3′ as forward primer and 5′-AAAGTCGCTCTG AGTTGTTAT-3′ as reverse primer (band size: 600 bp). On the other hand, the *Rosa26*^{lsl}*-Cmah* gene was determined using 5^{0}-ATTCT AGTTGTGGTTTGTCC-3′ and 5′-ATGGTGCTCACGTCTAACTTCC-3′ primers (band size: 370 bp).

Floxed *Cd22* mice (*C57BL/6N-Cd22tm1a(EUCOMM)Wtsi/Tcp*) were rederived from sperm acquired through The Centre for Phenogenomics (Toronto, Canada). Initially, mice hemizygous for the tm1a allele were established and crossed with Flp elete mice (B6.129S4-*Gt(ROSA)26Sortm2(FLP*)Sor*/J) from The Jackson Laboratory. Successful conversion of the tm1a allele into the tm1c allele of mouse *Cd22*, which we denote as *Cd22*$^{f/f}$, was verified by PCR for the presence of a proximal *loxP* site (primers: 5′-AAACAG CATGGGCTCTGCTTCACAG-3′ and 5′-TGGAGAGGCAAGCAAAGATGGAGAGG-3′; band size: 102 bp) and distal *loxP* site (primers: 5′-GCGCAACGCAATTAATGATAAC-3′ and 5′-TACAGTCATTTGAAAGAGGCCAGC-3′; band size: 211 bp). The WT *Cd22* locus was identified using 5′-GCGGGAAGGGACTGGCTGCTAT-3′ and 5′-AGTCCAGAGACCATCGGCAAG-3′ primers (band size: 270 bp), which also recognized the tm1c allele. Mice were subsequently backcrossed onto C57BL/6J mice to remove the flp recombinase and crossed with the relevant strains expressing Cre to generate mice homozygous for *Cd22*$^{f/f}$ and bearing either *Mb1*^{Cre} or *Aicda*^{Cre}.

All mice used in this study were bred and maintained under specific pathogen-free conditions. Experiments described in the study were approved by the Health Sciences Animal Care and Use Committee of the University of Alberta.

METHOD DETAILS

Bone marrow chimera and adoptive transfer—To generate mouse chimeras, WT recipients were irradiated with 1000 rad and injected intravenously with isolated bone marrow cells from various donor mice within 24 h. Single chimeras were carried out to control the age and sex of the mice for large cohort. Mixed bone marrow chimera mice were generated by reconstituting lethally irradiated WT mice with 1:1 ratio, unless otherwise specified, of bone marrow cells from indicated donor mice. For mixed chimeras with WT and $CD22^{KO}$ BM, a ratio of 1:2 (WT:$CD22^{KO}$) was used. Chimera mice were used after 7–10 weeks following bone marrow transplantation. For adoptive transfer of HEL-specific B-cells, B-cells from spleens of Hy10 mice were isolated using a mouse B-cell negative-isolation kit (Miltenyi). Approximately 1×10^6 splenic B-cells were injected into B6 recipient mice intravenously a day before immunization.

Cell lines—Human embryonic kidney (HEK) 293 T cells were acquired from ATCC and cultured in DMEM media supplemented with 10% fetal bovine serum (FBS; Gibco) and 100 U/mL of penicillin and 100 μg/mL streptomycin (Gibco). Chinese hamster ovary (CHO) Flp-In cells (Invitrogen) were maintained in DMEM-F12 media supplemented with 5% FBS, 100 U/mL of penicillin/100 μg/mL streptomycin, and 10 mM HEPES. The CD40LB feeder cell line was a gift from Dr. Daisuke Kitamura (Tokyo University of Science, Japan) and Dr. Javier Marcelo Di Noia (University of Montreal, Canada). Feeder cells were cultured in DMEM supplemented with 10% FBS and 100 U/mL of penicillin/100 μg/mL streptomycin.

Liposome preparation, immunization, and tamoxifen administration—Liposomal nanoparticle-based immunogens give a robust and consistent T-cell-dependent antibody response, while avoiding the inclusion of a TLR agonist (Allison and Gregoriadis, 1974; Taneichi et al., 2002; Wang et al., 2019). Given that Siglecs, such as CD22, can interact and modulate toll-like receptor (TLR) function (Chen et al., 2014; Kawasaki et al., 2011), liposomes were used to minimize any confounding factors affecting the primary response to T-dependent antigens. Lyophilized lipids containing a 65:35:5 molar ratio of distearoyl phosphatidylcholine (DSPC) (Avanti Polar Lipids), cholesterol (Sigma), and PEG_{2000}-distearoyl phosphoethanolamine (PEG_{2000}-DSPE; Avanti Polar Lipids) were hydrated in sterile PBS and sonicated for a minimum of 20 min. NP-OVA-PEG_{2000}-DPSE, OVA-PEG_{2000}-DPSE or HEL-PEG_{2000}-DPSE, which were generated using a previously published protocol (Macauley et al., 2013), was added to the lipid mixture at the time of hydration. The molar fraction of Protein-PEG_{2000}-DPSE were maintained at 0.03% in all liposome preparations. Following sonication, liposomes were passed at least 15 times through 800 nm and 100 nm filters using a hand-held extrusion device (Avanti Polar Lipids). Excess Protein-PEG_{2000}-DPSE was separated from liposomes using a CL-4B Sepharose (Sigma) column. Eluted liposomes were diluted in sterile PBS to 1 mM concentration prior to administration to mice.

For immunization involving liposomes, each mouse received 200 μL of 1 mM liposomes via tail vein injection. Where indicated, at day 11 post-immunization (PI) with OVA-liposomes, mice were boosted with 10 μg of anti-DEC205-OVA, prepared according to a published

study (Pasqual et al., 2015), via tail vein injection. Spleens were collected at different time points PI for microscopy and flow cytometric analyses of the GC.

For temporal expression of human CD20-driven Cre recombinase, mouse chimeras reconstituted with *CD20-ERT2^{Cre}* and *CD20-ERT2^{Cre}×R26^{lsl}-Cmah* BM cells were gavaged with 1 mg tamoxifen (Combi-Blocks) in 200 μL corn oil (Sigma) on days 8 and 9 PI with OVA displaying liposomes. Spleens were collected on Day 14 (5 days post-tamoxifen) for flow cytometric analysis of GC B-cells.

Flow cytometry and sorting—Spleens were macerated in RPMI 1640 containing 2% FBS and passed through a 40 μm mesh. Single cell suspensions were treated with Ammonium-Chloride-Potassium (ACK) lysis buffer for five minutes at 4°C to deplete red blood cells (RBC). RBC-depleted splenocytes were washed and resuspended in HBSS containing 2% FBS or 0.1% bovine serum albumin (flow buffer). Aliquots of cell suspensions were stained on ice for 30 min using appropriate reagents and surface marker antibodies as listed in the key resource table. Stained cells were washed and resuspended in flow buffer supplemented with 1 μg/mL of viability dye propidium iodide or 7-AAD. Naive and GC B-cell compartments were gated on a Fortessa X-20 flow cytometer as $B220^{+}CD19^{+}IgD^{+}$ and $B220^{+}CD19^{+}IgD^{-}CD38^{low}Fas^{+}GL7^{+}$ (or PNA^{+}) live single cells, respectively, unless specified otherwise. OVA-specific GC B-cells were further gated on the flow cytometer using OVA-AF647 (Invitrogen). NP^{+} GC B-cells were determined in flow using NP_{20}-APC and NP_{4}-APC (prepared according to protocol provided by Dr. Pierre Milpied of CIML, France). Dark zone and light zone compartments were identified as $CXCR4^{high}CD86^{low}$ and $CXCR4^{low}CD86^{high}$ GC B-cells, respectively.

For active-caspase-3 staining, cells stained with surface marker antibodies were fixed and permeabilized with BD Cytofix/Cytoperm™ (BD Biosciences) on ice for 20 min. Fixed cells were washed two times with flow buffer, followed by incubation with intra-cellular marker antibodies for 30 min at 4°C.

For nuclear and phosphorylated protein (phosFlow) staining, cells were fixed in 2% of paraformaldehyde at room temperature for 10 min. Fixed cells were wash with flow buffer twice followed by incubation with True-Nuclear™ Transcription Factor permeabilization buffer (BioLegend), following the manufacturer's recommended protocol. Fixed/permeabilized cells were wash twice with flow buffer and stained with both surface and intracellular markers for 1 h at 4°C.

For cell cycle and proliferation assays, immunized mice were injected intravenously with 1 mg BrdU (Sigma) dissolved in sterile PBS. Spleens were harvested after 1 h and RBC-depleted single cell suspensions were stained with surface marker antibodies for naive and GC B-cells for 30 min at 4°C. Following incubation, cells were washed with flow buffer and fixed with BD Cytofix/Cytoperm™ for 20 min at 4°C. Cells were then washed 2 times with flow buffer and incubated with BD Cytoperm™ Permeabilization Buffer Plus (BD Biosciences) for 10 min at 4°C. Cells were washed twice with flow buffer, re-fixed with BD Cytofix/Cytoperm™ for 10 min at 4°C, and incubated at 37°C with 20 μg/mL of DNase I (Sigma) in PBS containing Ca^{2+} and Mg^{2+}. Following incubation, cells were washed and

stained with anti-BrdU antibody (BioLegend) and 7-AAD for 20 min at room temperature. Proliferating cells were gated on the flow cytometer as $BrdU^+$ B-cells. Cell cycle phases of GC B-cells were identified as described previously (Pozarowski and Darzynkiewicz, 2004).

For sorting GC B-cells, RBC-depleted splenocytes were stained with appropriate surface marker antibodies in HBSS containing 2% of FBS and 1 mM EDTA (FACS buffer) for 30 min at 4°C. Cells were washed and resuspended in FACS buffer supplemented with 1 μg/mL 7-AAD. GC B-cells were sorted by BD FACS Aria III (BD Biosciences) using a 100-μm nozzle. Sorted single cells were then collected in cold RPMI 1640 media containing 10% FBS, $5.5 \times 10^{—5}$ M 2-mercaptoethanol (Sigma), 10 μM HEPES (Gibco), 1 mM sodium pyruvate (Gibco), 1 mM essential amino acids (Gibco), 100 U/mL of penicillin and 100 μg/mL streptomycin.

Immunofluorescence—Spleens from non-immunized and immunized mice were embedded in cryomatrix (Thermo Fisher), froze, and stored at —80°C prior to sectioning. Cryostat tissue sections (9 μm) were fixed and permeabilized in a cold 1:1 mixture of acetone and methanol for 5 min, blocked with HBSS supplemented with 5% FBS for 40 min at room temperature, and washed with PBS-T. Tissue sections were then stained with lectin PNA-biotin (Vector Lab) and antibodies GL7-biotin (BioLegend), anti-mouse IgD (clone: 11.26c.2a; Bio-Legend), anti-mouse CD21/35 (clone: 7G6; BD Biosciences) in different combinations overnight at 4°C.The following day, tissue sections were washed 3 times with PBS-T and the following secondary antibodies were used to detect the primary antibodies: Streptavidin-AF555 (Invitrogen), anti-rat IgG2a-AF488 (SouthernBiotech), and anti-rat IgG2b-AF647 (BioLegend). Following incubation, tissue sections were washed 5 times with PBST and stained with 2.5 μg/mL Hoechst for 15 min at room temperature. Images of spleen sections were acquired with either Zeiss LSM700 microscope (20× magnification) or Molecular Devices ImageXpress Pico (10× magnification). Individual GC clusters were imaged with Zeiss LSM700 confocal microscope using 63× magnification. Image analysis was performed using ZEN Blue and Fiji processing software.

Enzyme-linked immunosorbent assay (ELISA)—To measure the affinity maturation of antigen-specific antibodies, sera were collected on days 14, 21, and 42 after immunization with 0.03% NP-OVA liposomal nanoparticles. High affinity NP-specific and total NP-specific antibodies were captured on plates precoated with 10 μg/mL of NP_2-BSA (prepared following the recommended protocol provided by Dr. Daisuke Kitamura) and NP_{23}-BSA (LGC Biosearch), respectively. Plates were washed 5 times with PBS-T and incubated with goat anti-mouse IgG1 antibody conjugated with horseradish peroxidase (SouthernBiotech) for 1 h at room temperature. Plates were then washed 5 times with PBS-T followed by addition of peroxidase substrate 2,2′-azino-bis(3-ethylbenzothiazoline-6-sulfonic acid) (ABTS) solution (Sera-Care) into each well for colour development. After 15 min, reactions were stopped with 1 M phosphoric acid. Optical density was collected using a microplate reader set to 405 nm.

RNAseq and transcriptome analysis—Total RNA from sorted GC B-cells of immunized WT and $CD22^{KO}$ mice was extracted using a RNeasy micro kit (Qiagen). Indexed cDNA libraries were generated using a SMART-Seq Stranded kit (Takara Bio) for

the Illumina platform and the quality of each constructed library was measured using a Bioanalyzer 2100 (Agilent). Paired-end 150 bp sequencing was performed on an Illumina HiSeq platform by Novogene. For transcriptome analysis, the quality of unaligned reads was first validated using FastQC v0.11.2 followed by the removal of Illumina adapters using Cutadapt v3.3 (Martin, 2011). Adapter-trimmed sequencing reads were mapped to the GRCm38/mm10 reference genome using HISAT2 (Kim et al., 2015). Aligned reads were counted and annotated to Gencode M25 (Frankish et al., 2019) using HTseq-count (Anders et al., 2015), followed by read count normalization and differential expression analysis by DESeq2 (Love et al., 2014). Differentially expressed genes (DEGs) were determined based on the Benjamini-Hochberg (BH) corrected p value %0.05. Gene enrichment analysis was performed on DEGs with an unadjusted p value ≤0.05 using EnrichR (Chen et al., 2013; Kuleshov et al., 2016; Xie et al., 2021) and default settings or directly from gene expression profile using GSEA version 4 (Subramanian et al., 2005). Significantly enriched gene sets were identified based on FDR p value <0.05.

Ig VH 186.2 DNA sequencing and mutation analysis—Approximately 30,000 GC B-cells ($B220^+CD19^+IgD^-GL7^+NP_{20}$-$APC^+$ live cells) were isolated using FACS from splenocytes of WT and $CD22^{KO}$ mice, at day 21 after immunization with NP-OVA liposomes. Genomic DNA was extracted using a DNA microprep kit (Qiagen). To sequence the V_H186.2 region, V_H186.2 was amplified from the extracted genomic DNA by PCR using 5′-AGCTGTATC ATGCTCTTCTTGGCA-3′ and 5′-AGATGGAGGCCAGTGAGGGAC-3′ as forward and reverse primers, respectively. PCR was performed following a previously published (Chen et al., 2017). PCR products were then cloned into a pBAD vector (Invitrogen) and transformed into chemically competent DH5α *E. coli* (NEB Biolabs). Plasmids were extracted from *E. coli* clones using a GeneJET plasmid miniprep kit (Thermo Fisher), and DNA was sequenced using a Sanger sequencer. Mutational analysis of the Ig V region was performed using the IMGT/V-QUEST tool (www.imgt.org).

Anti-DEC205-OVA plasmids and recombinant protein expression and purification—Plasmids encoding the anti-DEC205 light chain and anti-DEC205 heavy chain fused to OVA were transformed into chemically competent DH5α *E. coli* and purified using a GeneJET plasmid miniprep kit (Thermo Fisher). To express anti-DEC205-OVA, HEK293 T cells were cultured in complete DMEM in T175 flasks and incubated at 37°C in a 5% CO_2 incubator until they reached approximately 70% confluence. HEK293 T cells in each flask were then added with 2 mL of OptiPro SFM containing 10 μg each of anti-DEC205 light chain and heavy chain plasmids, and 40 μg of branched polyethylenimine (Sigma) and incubated overnight at 37°C. The following day, the media were replaced with fresh complete DMEM and cultured for another 48–72 h. Media were collected, filter sterilized, and stored at 4°C prior to purification. Anti-DEC205-OVA was purified from the media using a HiTrap Protein G HP column (GE Healthcare) according to the manufacturer's recommendation, dialyzed in PBS, and quantified as described previously (Pasqual et al., 2015).

Generation of mouse CD22-Fc fusion—To generate the mouse CD22-Fc fusion, DNA encoding 1–435 amino acid residues of mouse CD22 was

amplified by PCR using 5′-AGCAGCGCTAGCATGCGCGTCCATTACCTGTGG-3′ and 5′-AGCAGCACCGGTATCCAGCTTAGCTTCCTG-3′ as forward and reverse primers, respectively. PCR products were cloned upstream of the human IgG1 Fc domain encoded in the pcDNA5/FRT/V5-His-TOPO® vector, which was described elsewhere (Rodrigues et al., 2020). Sequence verified plasmid encoding for mCD22-Fc was transfected together with Flp recombinase-expressing plasmid pOG44 (Invitrogen) using lipofectamine LTX (Invitrogen) into chinese hamster ovary (CHO) Flp-In cells. Stably transfected cells were selected after 10 days of culturing in DMEM-F12 containing 5% FBS, 100 U/mL of penicillin/100 μg/mL streptomycin, 2.438 g/L sodium bicarbonate (Gibco) and 1 μg/mL Hygromycin B (Invitrogen). For expression of mCD22-Fc, approximately 1×10^6 of mCD22-Fc expressing CHO cells were plated onto a T175 flask in DMEM-F12 media supplemented with 5% FBS, 100 U/mL of penicillin/100 μg/mL streptomycin, and 10 mM HEPES. Cells were then incubated at 37°C for 10–12 days. Supernatant from cultured cells was collected and filtered using a Rapid-Flow™ sterile filter with 0.2 μm PES membrane pore size (Nalgene).

To generate a non-binding mutant of mouse CD22-Fc (mCD22 R124A-Fc), site-directed mutagenesis was performed on the sialic acid-binding region of CD22 using a megaprimer-PCR strategy (Forloni et al., 2019). Briefly, the megaprimer containing the R124A mutation was generated by PCR using 5′-AGCAGCGCTAGCATGCGCGTCCATTACCTGTGG-3′ as the forward primer and 5′-AGTCCCTGCGGTCATGGCCAACCCCAGATTCCC-3′ as the reverse primer. A second round of PCR was performed to amplify the 1–435 amino acid residues of mouse CD22 containing the R124A mutation, using the megaprimer and 5′-AGCAGCACCGGTATC CAGCTTAGCTTCCTG-3′ as the forward and reverse primers, respectively. Cloning and protein expression of mCD22 R124A-Fc follow the same protocol as mentioned above.

***In vitro* GC B-cell culture—**For induction of GC B-cells *in vitro*, B-cells were isolated from mouse spleens using FACS or a mouse B-cell isolation kit (Miltenyi) and co-cultured with CD40LB fibroblast feeder lines in RPMI 1640 medium supplemented with 10% FBS, 5.5×10^{-5} M 2-mercaptoethanol, 10 mM HEPES, 1 mM sodium pyruvate, 1 mM essential amino acids, 100 U/mL of penicillin, and 100 μg/mL streptomycin. Mouse IL-4 (1 ng/mL; BioLegend) was added to primary co-culture for 4 days. Induced GC B-cells were then replated onto a fresh CD40LB feeder line and cultured with mouse IL-21 (10 ng/mL; BioLegend) or mouse IL-4 for another 3 to 4 days.

Intracellular Ca^{2+} mobilization—Approximately 15×10^6 splenocytes from mice, at day 14 after immunization, were resuspended in HBSS (Gibco) supplemented with 1% FBS and 1 μM Indo-1 AM (Invitrogen), and incubated at 37°C for 30 min. Cells were washed with a 5-fold volume of HBSS with 1% FBS and centrifuge at 300 rcf for 5 min. Pelleted cells were stained with surface marker lectin PNA and antibodies against mouse B220, CD38, CD45.1, and CD45.2 for 20 min at 4°C. Cells were washed and resuspended in HBSS containing 1% FBS. A 0.5 mL aliquot containing approximately 1×10^6 splenocytes was incubated for 5 min at 37°C prior to the Ca^{2+} mobilization assay. Ca^{2+} mobilization in GC and non-GC B-cells populations was detected using a Fortessa X-20 flow cytometer. After baseline was established (approximately 2–3 min), splenocytes were stimulated with buffer

(1% FBS/HBSS) or 10 μg/mL goat F(ab')$_2$ anti-mouse Igκ (SouthernBiotech) and Indo-1 fluorescence (violet vs blue) was monitored by flow cytometry for 3–5 min at 37°C. Data were analyzed using the kinetics function on FlowJo v 9.

***Ex vivo* antigen internalization and processing assay—**For the BCR internalization assay, RBC-depleted splenocytes were incubated with 1 μg/mL of goat F(ab')$_2$ anti-mouse Igκ-biotin (SouthernBiotech) for 30 min at 4°C. Splenocytes were washed 3 times with cold HBSS containing 0.1% BSA and resuspended in pre-warmed (37°C) RPMI 1640 medium supplemented with 10% FBS, 5.5 × 10^{-5} M 2-mercaptoethanol, 10 mM HEPES, 1 mM sodium pyruvate, 1 mM essential amino acids, 100 U/mL of penicillin, and 100 μg/mL streptomycin. Cells were then incubated in a 5% CO_2 incubator at 37°C for specified timepoints. At the end of each time point, cells were immediately fixed in 1% paraformaldehyde (PFA) for 10 min at room temperature. Fixed cells were washed 3 times with 0.1% BSA in HBSS followed by incubation of surface marker antibodies and fluorochrome-conjugated streptavidin. Changes in the levels of anti-mouse Igκ-biotin on fixed naive and GC B-cells were monitored by flow cytometer.

For the antigen degradation assay, splenocytes from immunized mice were stained with 1 μg/mL of goat F(ab')$_2$ anti-mouse Igκ-biotin followed by 1 μg/mL of streptavidin (BioLegend) at 4°C. Cells were washed 3 times with HBSS containing 0.1% BSA and incubated with 100 nM of a previously described biotin-conjugated antigen degradation sensor (Nowosad et al., 2016) at 4°C for 20 min. The degradation sensor consists of a fluorescent strand sequence: 5′-Atto647N-TCCGGCTGCCTCGCTGCCGTCGCCA-3′-biotin and a quencher strand sequence: 5′-TGGCGACGGCAGCGAGGCAGCCGGA-3′′-Iowa Black RQ. For sensor binding assays, the quencher strand sequence was replaced with 5′-TGGCGACGGCAGCGAGGCAGCCGGA-3′ instead. Stained cells were then washed 3 times, resuspended in pre-warmed RPMI 1640 medium supplemented with 10% FBS, 5.5 × 10^{-5} M 2-mercaptoethanol, 10 mM HEPES, 1 mM sodium pyruvate, 1 mM essential amino acids, 100 U/mL of penicillin, and 100 μg/mL streptomycin, and incubated in a 5% CO_2 incubator at 37°C for specified timepoints. After each time point, cells were fixed and stained with GC B-cell relevant surface marker antibodies. Changes in the fluorescence of the antigen degradation sensor were measured by flow cytometry.

QUANTIFICATION AND STATISTICAL ANALYSIS—All statistical analyses in this study were done with GraphPad Prism software except for the calculation of statistical significance of DEGs and enriched pathways, which were both performed in DESeq2 (Love et al., 2014), EnrichR (Chen et al., 2013; Kuleshov et al., 2016; Xie et al., 2021), and GSEA version 4 (Subramanian et al., 2005). For experiments comparing two groups, a two-tailed Student's t-test was used to evaluate statistical significance. When the assay was carried out in competition, a paired Student's t test was used; while an unpaired Student's t test was performed for samples analyzed independently. For experiments with more than 2 sample groups, a one-way or two-way analysis of variance (ANOVA) were performed to assess differences between means. Tukey or Dunnett multiple comparisons tests were used to determine statistical significance between groups.

Supplementary Material

Refer to Web version on PubMed Central for supplementary material.

ACKNOWLEDGMENTS

We thank Dr. Kitamura (Tokyo University of Science) and Dr. Marcelo Di Noia (University of Montreal) for providing the CD40L feeder cell lines; Dr. Pae and Dr. Victora (Rockefeller University) for providing αDEC205-OVA plasmids and bone marrow cells from *Cd205*^{KO} mice; Dr. Cyster (University of California [UC], San Francisco) for access to Hy10 mice; and Mr. Subedi of the Applied Genomics Core (University of Alberta) for help processing RNA. We thank Drs. Milpied (Centre d'Immunologie de Marseille-Luminy) and Lesage (Maisonneuve-Rosemont Hospital) for critical reading and feedback of our manuscript. This study was supported by grants from the NIH (R01AI118842 and R01AI050143) and the NSERC (RGPIN-2018–03815) and a Canada Research Chair in Chemical Glycoimmunology to M.S.M. J.R.E. is funded by fellowships from the Alberta Innovates Graduate Student Scholarships and Canadian Arthritis Society.

REFERENCES

Adachi T, Wienands J, Wakabayashi C, Yakura H, Reth M, and Tsubata T (2001). SHP-1 requires inhibitory co-receptors to down-modulate B cell antigen receptor-mediated phosphorylation of cellular substrates. J. Biol. Chem 276, 26648–26655. [PubMed: 11356834]

Akkaya M, Traba J, Roesler AS, Miozzo P, Akkaya B, Theall BP, Sohn H, Pena M, Smelkinson M, Kabat J, et al. (2018). Second signals rescue B cells from activation-induced mitochondrial dysfunction and death. Nat. Immunol 19, 871–884. [PubMed: 29988090]

Allen CDC, Okada T, and Cyster JG (2007). Germinal-center organization and cellular dynamics. Immunity 27, 190–202. [PubMed: 17723214]

Allison AC, and Gregoriadis G (1974). Liposomes as immunological adjuvants. Nature 252, 252.

Alsadeq A, Hobeika E, Medgyesi D, Kläsener K, and Reth M (2014). The role of the Syk/Shp-1 kinase-phosphatase equilibrium in B cell development and signaling. J. Immunol 193, 268–276. [PubMed: 24899508]

Anders S, Pyl PT, and Huber W (2015). HTSeq—a Python framework to work with high-throughput sequencing data. Bioinformatics 31, 166–169. [PubMed: 25260700]

Bakker TR, Piperi C, Davies EA, and Merwe PA (2002). Comparison of CD22 binding to native CD45 and synthetic oligosaccharide. Eur. J. Immunol 32, 1924–1932. [PubMed: 12115612]

Bednar KJ, Shanina E, Ballet R, Connors EP, Duan S, Juan J, Arlian BM, Kulis MD, Butcher EC, Fung-Leung W-P, et al. (2017). Human CD22 inhibits murine B cell receptor activation in a human CD22 transgenic mouse model. J. Immunol 199, 3116–3128. [PubMed: 28972089]

Berek C, Berger A, and Apel M (1991). Maturation of the immune response in germinal centers. Cell 67, 1121–1129. [PubMed: 1760840]

Bhattacherjee A, Jung J, Zia S, Ho M, Eskandari-Sedighi G, Laurent CD St., McCord KA, Bains A, Sidhu G, Sarkar S, et al. (2021). The CD_{33} short isoform is a gain-of-function variant that enhances Ab1–42 phagocytosis in microglia. Mol. Neurodegener 16, 19. [PubMed: 33766097]

Bléry M, Tze L, Miosge LA, Jun JE, and Goodnow CC (2006). Essential role of membrane cholesterol in accelerated BCR internalization and uncoupling from NF-kB in B cell clonal anergy. J. Exp. Med 203, 1773–1783. [PubMed: 16801401]

Calado DP, Sasaki Y, Godinho SA, Pellerin A, Köchert K, Sleckman BP, de Alborá n IM, Janz M, Rodig S, and Rajewsky K (2012). MYC is essential for the formation and maintenance of germinal centers. Nat. Immunol 13, 1092–1100. [PubMed: 23001146]

Cao A, Alluqmani N, Buhari FHM, Wasim L, Smith LK, Quaile AT, Shannon M, Hakim Z, Furmli H, Owen DM, et al. (2018). Galectin-9 binds IgM-BCR to regulate B cell signaling. Nat. Commun 9, 3288. [PubMed: 30120235]

Chappell CP, Draves KE, and Clark EA (2017). CD22 is required for formation of memory B cell precursors within germinal centers. PLoS One 12, e0174661. [PubMed: 28346517]

Chen EY, Tan CM, Kou Y, Duan Q, Wang Z, Meirelles GV, Clark NR, and Ma'ayan A (2013). Enrichr: interactive and collaborative HTML5 gene list enrichment analysis tool. BMC Bioinformatics 14, 128. [PubMed: 23586463]

Chen G-Y, Brown NK, Wu W, Khedri Z, Yu H, Chen X, van de Vlekkert D, D'Azzo A, Zheng P, and Liu Y (2014). Broad and direct interaction between TLR and Siglec families of pattern recognition receptors and its regulation by Neu1. Elife 3, e04066. [PubMed: 25187624]

Chen J, Cai Z, Zhang L, Yin Y, Chen X, Chen C, Zhang Y, Zhai S, Long X, Liu X, et al. (2017). Lis1 regulates germinal center B cell antigen acquisition and affinity maturation. J. Immunol 198, 4304–4311. [PubMed: 28446568]

Chou H-H, Takematsu H, Diaz S, Iber J, Nickerson E, Wright KL, Muchmore EA, Nelson DL, Warren ST, and Varki A (1998). A mutation in human CMP-sialic acid hydroxylase occurred after the Homo-Pan divergence. Proc. Natl. Acad. Sci. U S A 95, 11751–11756. [PubMed: 9751737]

Collins BE, Blixt O, DeSieno AR, Bovin N, Marth JD, and Paulson JC (2004). Masking of CD22 by cis ligands does not prevent redistribution of CD22 to sites of cell contact. Proc. Natl. Acad. Sci. U S A 101, 6104–6109. [PubMed: 15079087]

Collins BE, Smith BA, Bengtson P, and Paulson JC (2006). Ablation of CD22 in ligand-deficient mice restores B cell receptor signaling. Nat. Immunol 7, 199–206. [PubMed: 16369536]

Comelli EM, Sutton-Smith M, Yan Q, Amado M, Panico M, Gilmartin T, Whisenant T, Lanigan CM, Head SR, Goldberg D, et al. (2006). Activation of murine CD4+ and CD8+ T lymphocytes leads to dramatic remodeling of N-linked glycans. J. Immunol 177, 2431–2440. [PubMed: 16888005]

De Gassart A, Camosseto V, Thibodeau J, Ceppi M, Catalan N, Pierre P, and Gatti E (2008). MHC class II stabilization at the surface of human dendritic cells is the result of maturation-dependent MARCH I down-regulation. Proc. Natl. Acad. Sci. U S A 105, 3491–3496. [PubMed: 18305173]

De Silva NS, and Klein U (2015). Dynamics of B cells in germinal centres. Nat. Rev. Immunol 15, 137–148. [PubMed: 25656706]

Dias AM, Pereira MS, Padrão NA, Alves I, Marcos-Pinto R, Lago P, and Pinho SS (2018). Glycans as critical regulators of gut immunity in homeostasis and disease. Cell Immunol 333, 9–18. [PubMed: 30049413]

Dominguez-Sola D, Victora GD, Ying CY, Phan RT, Saito M, Nussenz-weig MC, and Dalla-Favera R (2012). c-MYC is required for germinal center selection and cyclic re-entry. Nat. Immunol 13, 1083–1091. [PubMed: 23001145]

Duan S, Koziol-White CJ, Jester WF, Smith SA, Nycholat CM, Macauley MS, Panettieri RA, and Paulson JC (2019). CD33 recruitment inhibits IgE-mediated anaphylaxis and desensitizes mast cells to allergen. J. Clin. Invest 129, 1387–1401. [PubMed: 30645205]

Ersching J, Efeyan A, Mesin L, Jacobsen JT, Pasqual G, Grabiner BC, Dominguez-Sola D, Sabatini DM, and Victora GD (2017). Germinal center selection and affinity maturation require dynamic regulation of mTORC1 kinase. Immunity 46, 1045–1058.e6. [PubMed: 28636954]

Forloni M, Liu AY, and Wajapeyee N (2019). Megaprimer polymerase chain reaction (PCR)-Based mutagenesis. Cold Spring Harb. Protoc 2019. 10.1101/pdb.prot097824.

Frankish A, Diekhans M, Ferreira A-M, Johnson R, Jungreis I, Loveland J, Mudge JM, Sisu C, Wright J, Armstrong J, et al. (2019). GENCODE reference annotation for the human and mouse genomes. Nucleic Acids Res 47, D766–D773. [PubMed: 30357393]

Furukawa K, Akasako-Furukawa A, Shirai H, Nakamura H, and Azuma T (1999). Junctional amino acids determine the maturation pathway of an antibody. Immunity 11, 329–338. [PubMed: 10514011]

Gasparrini F, Feest C, Bruckbauer A, Mattila PK, Müller J, Nitschke L, Bray D, and Batista FD (2016). Nanoscale organization and dynamics of the siglec CD22 cooperate with the cytoskeleton in restraining BCR signalling. EMBO J 35, 258–280. [PubMed: 26671981]

Getahun A, Beavers NA, Larson SR, Shlomchik MJ, and Cambier JC (2016). Continuous inhibitory signaling by both SHP-1 and SHIP-1 pathways is required to maintain unresponsiveness of anergic B cells. J. Exp. Med 213, 751–769. [PubMed: 27114609]

Haga CL, Ehrhardt GRA, Boohaker RJ, Davis RS, and Cooper MD (2007). Fc receptor-like 5 inhibits B cell activation via SHP-1 tyrosine phosphatase recruitment. Proc. Natl. Acad. Sci. U S A 104, 9770–9775. [PubMed: 17522256]

Hobeika E, Thiemann S, Storch B, Jumaa H, Nielsen PJ, Pelanda R, and Reth M (2006). Testing gene function early in the B cell lineage in mb1-cre mice. Proc. Natl. Acad. Sci. U S A 103, 13789–13794. [PubMed: 16940357]

Irie A, Koyama S, Kozutsumi Y, Kawasaki T, and Suzuki A (1998). The molecular basis for the absence of N-glycolylneuraminic acid in humans. J. Biol. Chem 273, 15866–15871. [PubMed: 9624188]

Ise W, Fujii K, Shiroguchi K, Ito A, Kometani K, Takeda K, Kawakami E, Yamashita K, Suzuki K, Okada T, et al. (2018). T follicular helper cell-germinal center B cell interaction strength regulates entry into plasma cell or recycling germinal center cell fate. Immunity 48, 702–715.e4. [PubMed: 29669250]

Johswich A, Longuet C, Pawling J, Rahman AA, Ryczko M, Drucker DJ, and Dennis JW (2014). N-glycan remodeling on glucagon receptor is an effector of nutrient sensing by the hexosamine biosynthesis pathway. J. Biol. Chem 289, 15927–15941. [PubMed: 24742675]

Kawasaki N, Rademacher C, and Paulson JC (2011). CD_{22} regulates adaptive and innate immune responses of B cells. J. Innate Immun 3, 411–419. [PubMed: 21178327]

Khalil AM, Cambier JC, and Shlomchik MJ (2012). B cell receptor signal transduction in the GC is short-circuited by high phosphatase activity. Science 336, 1178–1181. [PubMed: 22555432]

Kim D, Langmead B, and Salzberg SL (2015). HISAT: a fast spliced aligner with low memory requirements. Nat. Methods 12, 357–360. [PubMed: 25751142]

Kimura N, Ohmori K, Miyazaki K, Izawa M, Matsuzaki Y, Yasuda Y, Takematsu H, Kozutsumi Y, Moriyama A, and Kannagi R (2007). Human B-lymphocytes express α2–6-sialylated 6-sulfo-N-acetyllactosamine serving as a preferred ligand for CD_{22}/siglec-2. J. Biol. Chem 282, 32200–32207. [PubMed: 17728258]

Kuleshov MV, Jones MR, Rouillard AD, Fernandez NF, Duan Q, Wang Z, Koplev S, Jenkins SL, Jagodnik KM, Lachmann A, et al. (2016). Enrichr: a comprehensive gene set enrichment analysis web server 2016 update. Nucleic Acids Res 44, W90–W97. [PubMed: 27141961]

Liu H, Jain R, Guan J, Vuong V, Ishido S, La Gruta NL, Gray DH, Villadangos JA, and Mintern JD (2016). Ubiquitin ligase MARCH 8 cooperates with CD_{83} to control surface MHC II expression in thymic epithelium and CD4 T cell selection. J. Exp. Med 213, 1695–1703. [PubMed: 27503069]

Liu Y-J, Joshua DE, Williams GT, Smith CA, Gordon J, and MacLennan ICM (1989). Mechanism of antigen-driven selection in germinal centres. Nature 342, 929–931. [PubMed: 2594086]

Love MI, Huber W, and Anders S (2014). Moderated estimation of fold change and dispersion for RNA-seq data with DESeq2. Genome Biol 15, 550. [PubMed: 25516281]

Luo W, Weisel F, and Shlomchik MJ (2018). B cell receptor and CD40 Signaling are Rewired for Synergistic induction of the c-Myc transcription factor in germinal center B cells. Immunity 48, 313–326.e5. [PubMed: 29396161]

Luo W, Hawse W, Conter L, Trivedi N, Weisel F, Wikenheiser D, Cattley RT, and Shlomchik MJ (2019). The AKT kinase signaling network is rewired by PTEN to control proximal BCR signaling in germinal center B cells. Nat. Immunol 20, 736–746. [PubMed: 31011187]

Macauley MS, Pfrengle F, Rademacher C, Nycholat CM, Gale AJ, von Drygalski A, and Paulson JC (2013). Antigenic liposomes displaying CD22 ligands induce antigen-specific B cell apoptosis. J. Clin. Invest 123, 3074–3083. [PubMed: 23722906]

Macauley MS, Kawasaki N, Peng W, Wang S-H, He Y, Arlian BM, McBride R, Kannagi R, Khoo K-H, and Paulson JC (2015). Unmasking of CD22 Co-receptor on germinal center B-cells occurs by alternative mechanisms in mouse and man. J. Biol. Chem 290, 30066–30077. [PubMed: 26507663]

Maeda A, Scharenberg AM, Tsukada S, Bolen JB, Kinet J-P, and Kurosaki T (1999). Paired immunoglobulin-like receptor B (PIR-B) inhibits BCR-induced activation of Syk and Btk by SHP-1. Oncogene 18, 2291–2297. [PubMed: 10327049]

Marth JD, and Grewal PK (2008). Mammalian glycosylation in immunity. Nat. Rev. Immunol 8, 874–887. [PubMed: 18846099]

Martin M (2011). Cutadapt removes adapter sequences from high-throughput sequencing reads. EMBnet. J 17, 10–12.

Mesin L, Ersching J, and Victora GD (2016). Germinal center B cell dynamics. Immunity 45, 471–482. [PubMed: 27653600]

Meyer SJ, Steffensen M, Acs A, Weisenburger T, Wadewitz C, Winkler TH, and Nitschke L (2021). CD_{22} controls germinal center B cell receptor signaling, which influences plasma cell and memory B cell output. J. Immunol 207, 1018–1032. [PubMed: 34330755]

Mueller J, Matloubian M, and Zikherman J (2015). Cutting edge: an in vivo reporter reveals active B cell receptor signaling in the germinal center. J. Immunol 194, 2993–2997. [PubMed: 25725108]

Müller J, Obermeier I, Wöhner M, Brandl C, Mrotzek S, Angermüller S, Maity PC, Reth M, and Nitschke L (2013). CD_{22} ligand-binding and signaling domains reciprocally regulate B-cell Ca2+ signaling. Proc. Natl. Acad. Sci. U S A 110, 12402–12407. [PubMed: 23836650]

Muramatsu M, Sankaranand VS, Anant S, Sugai M, Kinoshita K, Davidson NO, and Honjo T (1999). Specific expression of activation-induced cytidine deaminase (AID), a novel member of the RNA-editing deaminase family in germinal center B cells. J. Biol. Chem 274, 18470–18476. [PubMed: 10373455]

Naito Y, Takematsu H, Koyama S, Miyake S, Yamamoto H, Fujinawa R, Sugai M, Okuno Y, Tsujimoto G, Yamaji T, et al. (2007). Germinal center marker GL7 probes activation-dependent repression of N-glycolylneuraminic acid, a sialic acid species involved in the negative modulation of B-cell activation. Mol. Cell Biol 27, 3008–3022. [PubMed: 17296732]

Naito-Matsui Y, Takada S, Kano Y, Iyoda T, Sugai M, Shimizu A, Inaba K, Nitschke L, Tsubata T, Oka S, et al. (2014). Functional evaluation of activation-dependent alterations in the sialoglycan composition of T cells. J. Biol. Chem 289, 1564–1579. [PubMed: 24297165]

Nojima T, Haniuda K, Moutai T, Matsudaira M, Mizokawa S, Shiratori I, Azuma T, and Kitamura D (2011). In-vitro derived germinal centre B cells differentially generate memory B or plasma cells in vivo. Nat. Commun 2, 1–11.

Nowosad CR, Spillane KM, and Tolar P (2016). Germinal center B cells recognize antigen through a specialized immune synapse architecture. Nat. Immunol 17, 870–877. [PubMed: 27183103]

Parker RB, and Kohler JJ (2010). Regulation of intracellular signaling by extracellular glycan remodeling. ACS Chem. Biol 5, 35–46. [PubMed: 19968325]

Pasqual G, Angelini A, and Victora GD (2015). Triggering positive selection of germinal center B cells by antigen targeting to DEC-205. Methods Mol. Biol 1291, 125–134. [PubMed: 25836306]

Porter AG, and Jänicke RU (1999). Emerging roles of caspase-3 in apoptosis. Cell Death Differ 6, 99–104. [PubMed: 10200555]

Pozarowski P, and Darzynkiewicz Z (2004). Analysis of cell cycle by flow cytometry. Methods Mol. Biol 281, 301–311. [PubMed: 15220539]

Ramya TNC, Weerapana E, Liao L, Zeng Y, Tateno H, Liao L, Yates JR, Cravatt BF, and Paulson JC (2010). In situ trans ligands of CD22 identified by glycan-protein photocross-linking-enabled proteomics. Mol. Cell Proteomics 9, 1339–1351. [PubMed: 20172905]

Rao SP, Vora KA, and Manser T (2002). Differential expression of the inhibitory IgG Fc receptor FcgRIIB on germinal center cells: implications for selection of high-affinity B cells. J. Immunol 169, 1859–1868. [PubMed: 12165510]

Reboldi A, and Dang E (2018). Cholesterol metabolism in innate and adaptive response. F1000Res 7, 1–9.

Robbiani DF, Bothmer A, Callen E, Reina-San-Martin B, Dorsett Y, Difilippantonio S, Bolland DJ, Chen HT, Corcoran AE, Nussenzweig A, et al. (2008). AID is required for the chromosomal breaks in c-myc that lead to c-myc/IgH translocations. Cell 135, 1028–1038. [PubMed: 19070574]

Rodrigues E, Jung J, Park H, Loo C, Soukhtehzari S, Kitova EN, Mozaneh F, Daskhan G, Schmidt EN, Aghanya V, et al. (2020). A versatile soluble siglec scaffold for sensitive and quantitative detection of glycan ligands. Nat. Commun 11, 5091. [PubMed: 33037195]

Sasi BK, Turkalj S, Kalkan H, Porro F, Bojnik E, Pyrzynska B, Zerrouqi A, Bobrowicz M, Winiarska M, Priebe V, et al. (2018). SHP1 deficiency is responsible for the constitutive activation of the BCR pathway in GCB DLBCL. Blood 132, 2860.

Sgroi D, Koretzky GA, and Stamenkovic I (1995). Regulation of CD_{45} engagement by the B-cell receptor CD22. Proc. Natl. Acad. Sci. U S A 92, 4026–4030. [PubMed: 7537381]

Shulman Z, Gitlin AD, Weinstein JS, Lainez B, Esplugues E, Flavell RA, Craft JE, and Nussenzweig MC (2014). Dynamic signaling by T follicular helper cells during germinal center B cell selection. Science 345, 1058–1062. [PubMed: 25170154]

Singh P, Saxena R, Srinivas G, Pande G, and Chattopadhyay A (2013). Cholesterol biosynthesis and homeostasis in regulation of the cell cycle. PLoS One 8, e58833. [PubMed: 23554937]

Subramanian A, Tamayo P, Mootha VK, Mukherjee S, Ebert BL, Gillette MA, Paulovich A, Pomeroy SL, Golub TR, Lander ES, et al. (2005). Gene set enrichment analysis: a knowledge-based approach for interpreting genome-wide expression profiles. Proc. Natl. Acad. Sci. U S A 102, 15545–15550. [PubMed: 16199517]

Taneichi M, Naito S, Kato H, Tanaka Y, Mori M, Nakano Y, Yamamura H, Ishida H, Komuro K, and Uchida T (2002). T cell-independent regulation of IgE antibody production induced by surface-linked liposomal antigen. J. Immunol 169, 4246–4252. [PubMed: 12370355]

Tsubata T (2018). Ligand recognition determines the role of inhibitory B cell Co-receptors in the regulation of B cell homeostasis and autoimmunity. Front. Immunol 9, 2276. [PubMed: 30333834]

Tu C-F, Wu M-Y, Lin Y-C, Kannagi R, and Yang R-B (2017). FUT8 promotes breast cancer cell invasiveness by remodeling TGF-b receptor core fucosylation. Breast Cancer Res 19, 111. [PubMed: 28982386]

Turner JS, Ke F, and Grigorova IL (2018). B cell receptor crosslinking augments germinal center B cell selection when T cell help is limiting. Cell Rep 25, 1395–1403.e4. [PubMed: 30403996]

Victora GD, and Nussenzweig MC (2012). Germinal centers. Annu. Rev. Immunol 30, 429–457. [PubMed: 22224772]

Wang N, Chen M, and Wang T (2019). Liposomes used as a vaccine adjuvant-delivery system: from basics to clinical immunization. J. Control. Release 303, 130–150. [PubMed: 31022431]

Xie Z, Bailey A, Kuleshov MV, Clarke DJB, Evangelista JE, Jenkins SL, Lachmann A, Wojciechowicz ML, Kropiwnicki E, Jagodnik KM, et al. (2021). Gene set knowledge discovery with enrichr. Curr. Protoc 1, e90. [PubMed: 33780170]

Yoshida H, Lareau CA, Ramirez RN, Rose SA, Maier B, Wroblewska A, Desland F, Chudnovskiy A, Mortha A, Dominguez C, et al. (2019). The cis-regulatory atlas of the mouse immune system. Cell 176, 897–912.e20. [PubMed: 30686579]

Highlights

- A mouse model ($CMAH^{ON}$) is made to test a role for altered glycosylation in the GC
- $CMAH^{ON}$ display a CD22-dependent defective GC response
- Altered glycosylation in the GC affects the ability of CD22 to regulate the BCR
- Altered glycosylation/CD22 play a role in antigen processing, survival, and selection

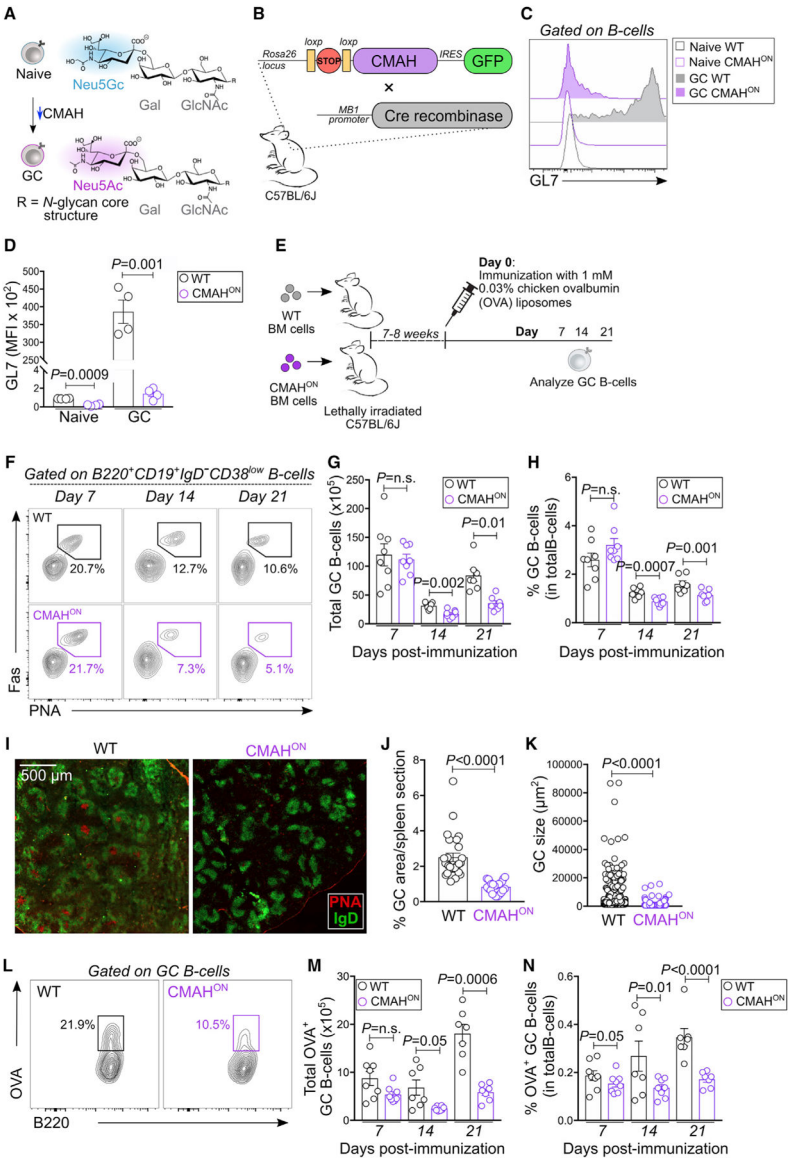

Figure 1. Constitutive expression of CMAH in GC B cells restricts GC B cell response following immunization

(A) CMAH-mediated changes in sialic acid during GC differentiation.

(B) *Cmah* transgenic mouse model developed for this study.

(C and D) Flow cytometric analysis of GL7 epitope expression on WT and CMAH transgene-expressing naive and GC B cells (C) and quantification of GL7 epitope levels (D). n = 4 mice/group.

(E) Immunization scheme of *R26*^{lsl}-*Cmah* (WT) and CMAH^{ON} chimera mice. Spleens were collected at various time points PI to analyze for GC B cells.

(F) Gating strategy for total GC B cells.

(G and H) Quantification of the absolute number (G) and percentage of GC B cells (H) of *R26*^{lsl}-*Cmah* (WT) and CMAH^{ON} GC B cells in immunized mouse spleens. An increase in GC B cell number on day 21 may be due to experimental difference in cell preparations. n = 7 or 8 mice/group and per time point.

(I) Immunofluorescence images of spleen section from immunized WT and CMAH^{ON} mice, at day 14 PI.

(J and K) Quantification of percentage GC area per spleen section (I) and GC cluster sizes (J) in spleens of immunized WT or CMAH^{ON} mice. n = 4 spleen sections/group.

(L) Flow cytometric gating strategy for identification of OVA-specific GC B cells in immunized *R26*^{lsl}-*Cmah* (WT) and CMAH^{ON} mice spleens.

(M and N) Quantification of the absolute number (M) and percentage of OVA-specific *R26*^{lsl}-*Cmah* (WT) and CMAH^{ON} GC B cells in spleens of immunized mice. n = 7 or 8 mice/group.

Data are presented as mean ± SEM. Statistical analysis was performed using unpaired Student's t test. n.s., not significant.

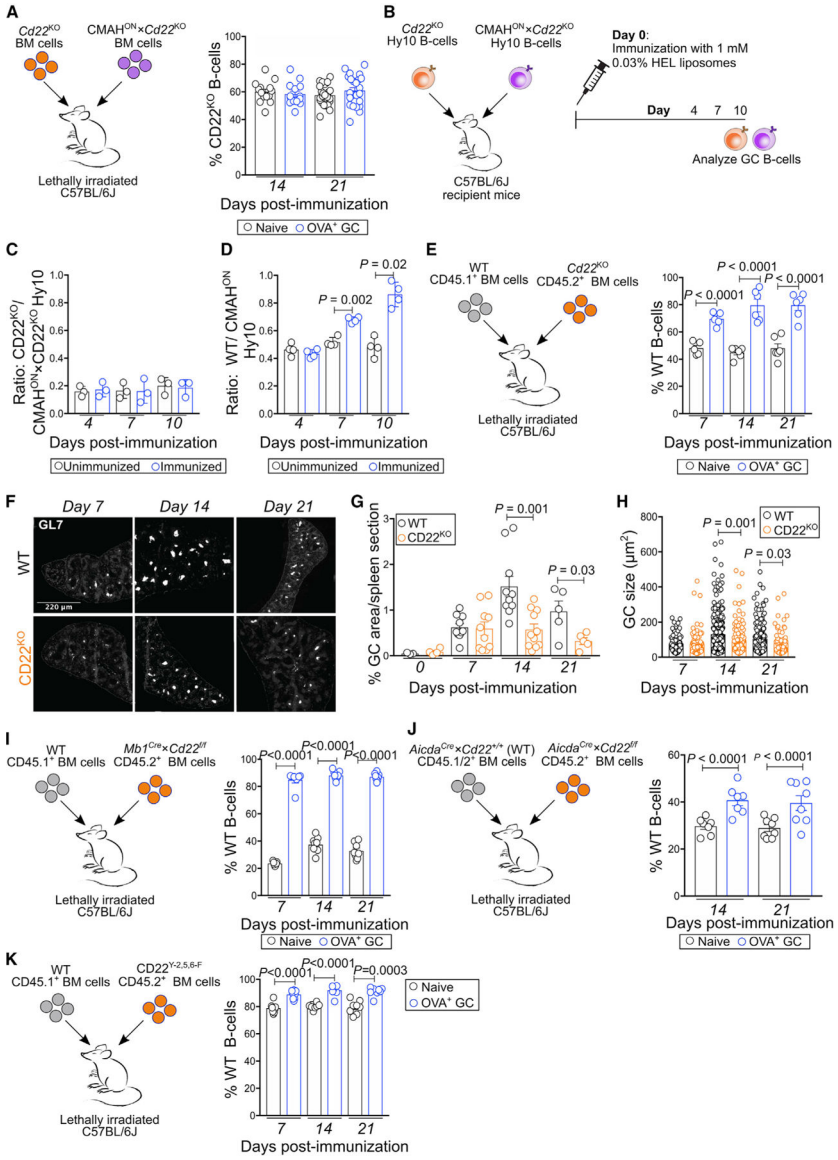

Figure 2. Restricted B cell response in CMAH-expressing GC B cells is dependent on CD22

(A) Quantification of percentage CD22^{KO} GC B cells in mixed bone marrow chimera mice reconstituted with BM cells from *Cd22*^{KO} and CMAH^{ON}×*Cd22*^{KO} donor mice, after days 14 and 21 PI.

(B) Scheme for the adoptive transfer of HEL-specific B cells and immunization with HEL liposomes. Pooled data from 3 independent experiments; n = 14 mice for day 14 and n = 22 mice for day 21.

(C and D) Quantification of percentage HEL-specific B cells in unimmunized and immunized mice that have been adoptively transferred with HEL-specific CD22^{KO} and CMAH^{ON}×*Cd22*^{KO} B cells (C) or HEL-specific WT and CMAH^{ON} B cells (D). n = 3 or 4 mice per time point.

(E) Quantification of percentage WT GC B cells in mixed bone marrow chimera mice, reconstituted with BM cells from CD45.1^{+} WT and CD22^{KO} donor mice, after days 7, 14, and 21 PI. n = 5 or 6 mice per time point.

(F–H) Immunofluorescence imaging of GCs (GL7^{+}) (F) and quantifications of percentage area covered by GC clusters/section (G) and size of GC clusters (H) in spleens of immunized WT and CD22^{KO} mice. WT n = 4–10 mice per time point, CD22^{KO} n = 4–11 mice per time point.

(I–K) Quantification of percentage WT GC B cells in mixed bone marrow chimera mice, reconstituted with BM cells from CD45.1^{+} WT and CMAH^{ON} donor mice (I), *Aicda*^{Cre}×*Cd22*$^{+/+}$ (as WT control) and *Aicda*^{Cre}×*Cd22*$^{f/f}$ donor mice (J), or CD45.1^{+} WT and CD22$^{Y-2,5,6\text{-}F}$ donor mice after days 7, 14, and 21 PI (K). n = 6–8 mice per time point. Data are presented as mean ± SEM. Statistical analysis was performed using paired Student's t test (A–E and I–K) or unpaired Student's t test (G and H).

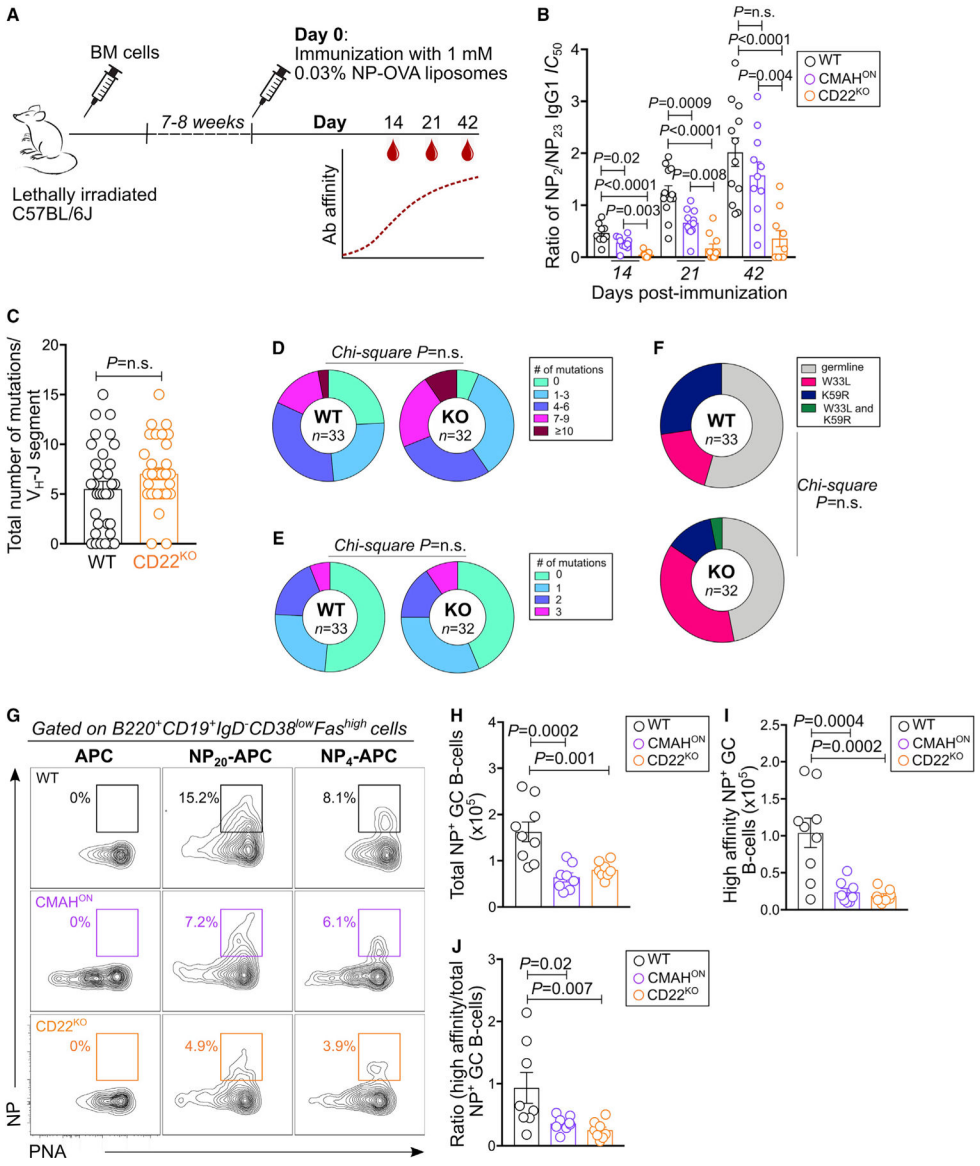

Figure 3. CD22 is not required in BCR SHM but is crucial for selection and/or maintenance of GC B cell clones and antibody affinity maturation

(A) Immunization procedure used to assess antibody affinity maturation.

(B) Affinity maturation of NP-specific IgG1 from sera of immunized WT, CMAH^{ON}, and CD22^{KO} mice collected at different time points PI. WT n = 12 mice, CMAH^{ON} n = 11 mice, and CD22^{KO} n = 8 mice.

(C) Quantification of total number of mutations in the V_H-J segment of NP$^+$ WT and CD22^{KO} GC B cells. n = 32 or 33 NP$^+$ GC B cells/group.

(D–F) Distribution of non-silent mutations present in the V region (D) and junction region (E) and affinity-enhancing mutations present in the V region (F) of NP$^+$ WT and CD22^{KO} GC B cells. n = 32 or 33 NP$^+$ GC B cells/group.

(G) Gating strategy used to determine the numbers of high-affinity NP$^+$ and total NP$^+$ GC B cells in spleens of immunized WT, CMAH^{ON}, and CD22^{KO} mice.

(H and I) Absolute numbers of total NP^+ (H) and high-affinity NP^+ (I) GC B cells present in spleens of immunized WT, $CMAH^{ON}$, and $CD22^{KO}$ mice. n = 8 or 9 mice/group.
(J) Ratio of high-affinity over total NP^+ GC B cells in immunized WT, $CMAH^{ON}$, and $CD22^{KO}$ mice. n = 8 or 9 mice/group.
Data are presented as mean ± SEM. Statistical analysis was performed using Tukey's multiple-comparison post one-way ANOVA (B and H–J), unpaired Student's t test (C), and chi-square probability test (D–F).

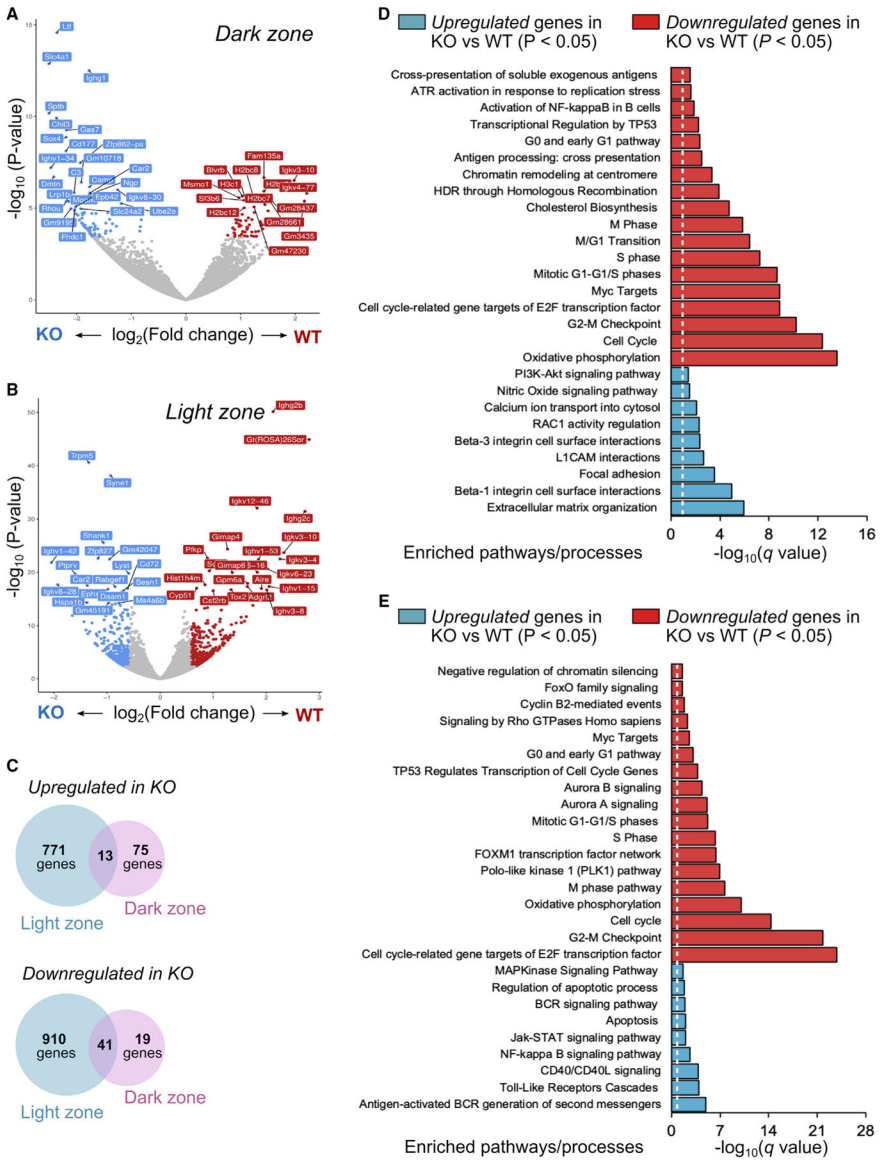

Figure 4. Transcriptional network reveals pathways dysregulated in CD22^{KO} GC B cells

(A) Volcano plot of dysregulated genes in DZ CD22^{KO} GC B cells n = 3 mice/group.

(B) Volcano plot of upregulated (blue) and downregulated genes in LZ CD22^{KO} GC B cells. n = 3 mice/group.

(C) Venn diagram showing the number of significantly dysregulated genes (Benjamini-Hochberg [BH]-corrected p < 0.05) in CD22^{KO} GC B cells.

(D) Gene set enrichment analysis of upregulated (blue) and downregulated genes in DZ CD22^{KO} GC B cells. n = 3 mice/group.

(E) Gene set enrichment analysis of upregulated (blue) and downregulated genes in LZ CD22^{KO} GC B cells. Vertical dashed lines represent BH q value = 0.05. n = 3 mice/group.

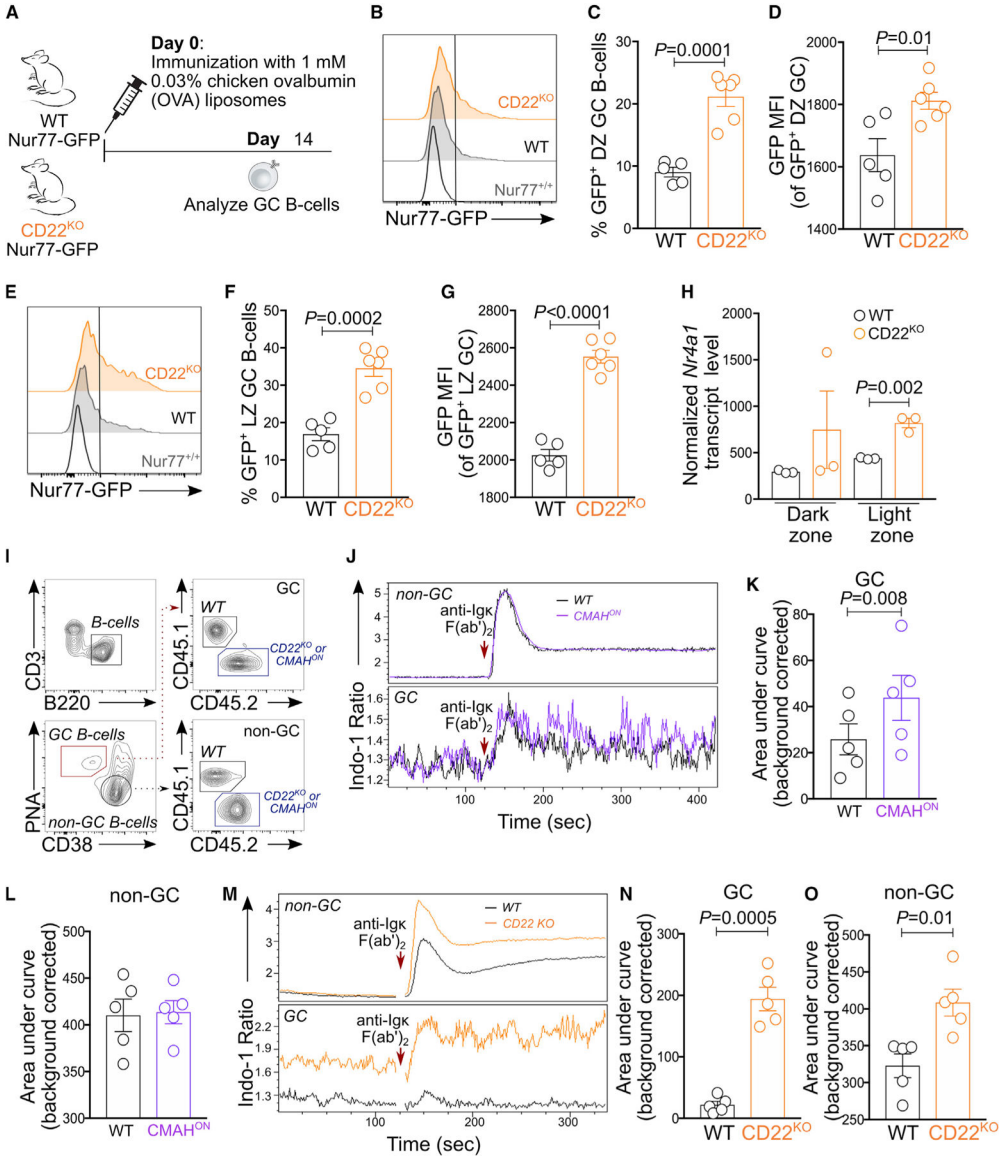

Figure 5. Loss of CD22 or sustained expression of CMAH hyperactivates B cell activation in the GC

(A) Scheme for immunization of WT and CD22^{KO} Nur77-GFP mice.

(B–D) Representative flow cytometric histogram of GFP expression in DZ GC compartment (B) and quantifications of percentage GFP^{+} B cells in WT and CD22^{KO} DZ GC compartment (C) as well as the GFP median fluorescence intensity (MFI) of GFP^{+} populations in WT and CD22^{KO} DZ GC B cells (D). n = 5 or 6 mice/group.

(E–G) Representative flow cytometric histogram of GFP expression in LZ GC compartment (E) and quantifications of percentage GFP^{+} B cells in WT and CD22^{KO} LZ GC compartment (F) as well as the GFP MFI of GFP^{+} populations in WT and CD22^{KO} LZ GC B cells (G). n = 5 or 6 mice/group.

(H) Normalized transcript levels of *Nr4a1* gene in DZ and LZ compartments of WT and CD22^{KO} GC B cells. n = 3 mice/group.

(I) Gating strategy for measurement of intracellular Ca^{2+} mobilization in GC B cells.

(J–L) Time-dependent analysis of Ca^{2+} flux between WT and $CMAH^{ON}$ B cells using Indo-1 (J). Area under the curve (AUC) is plotted for GC (K) and non-GC (L) compartments. n = 5 mice/group.
(M–O) Time-dependent analysis of Ca^{2+} flux between WT and $CD22^{KO}$ B cells (M). AUC is plotted for GC (N) and non-GC (O) compartments. n = 5 mice/group. Data are presented as mean ± SEM. Statistical analysis was performed using unpaired Student's t test (C, D, and F–H) and paired Student's t test (K, L, N, and O).

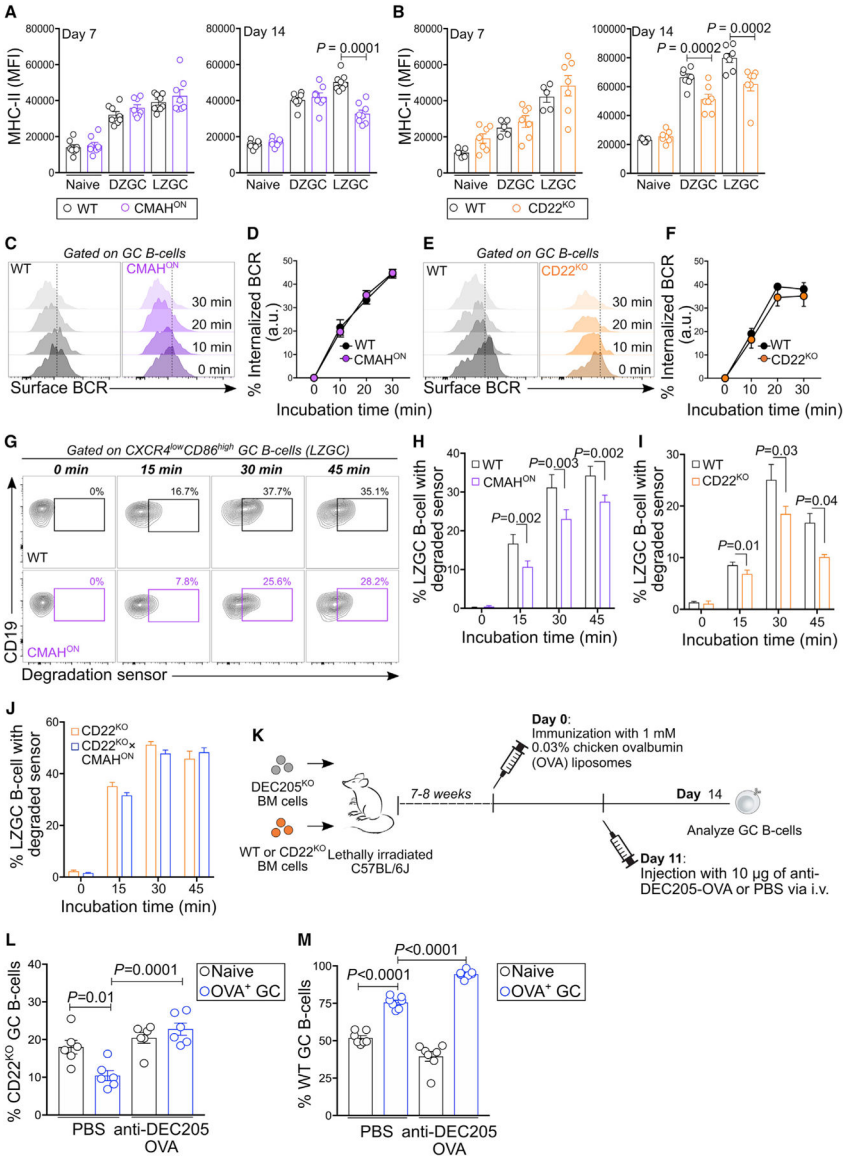

Figure 6. Impact of CD22 on MHC-II expression, BCR internalization, and antigen degradation

(A and B) Expression of MHC-II on WT and CMAH^{ON} naive, DZ, and LZ GC B cells (A) or WT and CD22^{KO} naive and GC B cells (B) on days 7 and 14 PI. n = 7 or 8 mice/group.

(C–F) Representative flow histograms (C and E) and quantification (D and F) of surface BCR of GC B cells from immunized mixed chimera mice reconstituted with WT and CMAH^{ON} (C and D) and WT and CD22^{KO} (E and F) mixed bone marrow cells, at different time points following BCR stimulation with goat F(ab′)$_2$ αmouse Igκ-biotin. n = 4 mice/group.

(G–J) Representative flow plots (G) and quantification (H–J) tracking the degradation of sensor at different time points post-BCR crosslinking and incubation at 37°C in WT and CMAH^{ON} (H), WT and CD22^{KO} (I), and CD22^{KO} and CD22^{KO}×CMAH^{ON} (J) LZ GC B cells. n = 4 mice/group.

(K) Scheme for administration of αDEC205-OVA or PBS in mixed BM chimera mice reconstituted with BM cells from $DEC205^{KO}$ and $CD22^{KO}$ donor mice.
(L and M) Quantification of the ratios of $CD22^{KO}$ naive and OVA^{+} GC B cells in chimera mice (L) or WT naive and OVA^{+} GC B cells in mixed chimera mice (WT and *Cd205*^{KO}) (M), 3 days after intravenous injection of either PBS (control) or αDEC205-OVA (day 14 PI). n = 6 or 7 mice/group.
Data are presented as mean ± SEM. Statistical analysis was performed using paired Student's t test (A, B, H, and I). One-way and two-way ANOVA was performed for (L) and (M) and for (D and F), respectively, followed by Tukey's test for multiple comparisons.

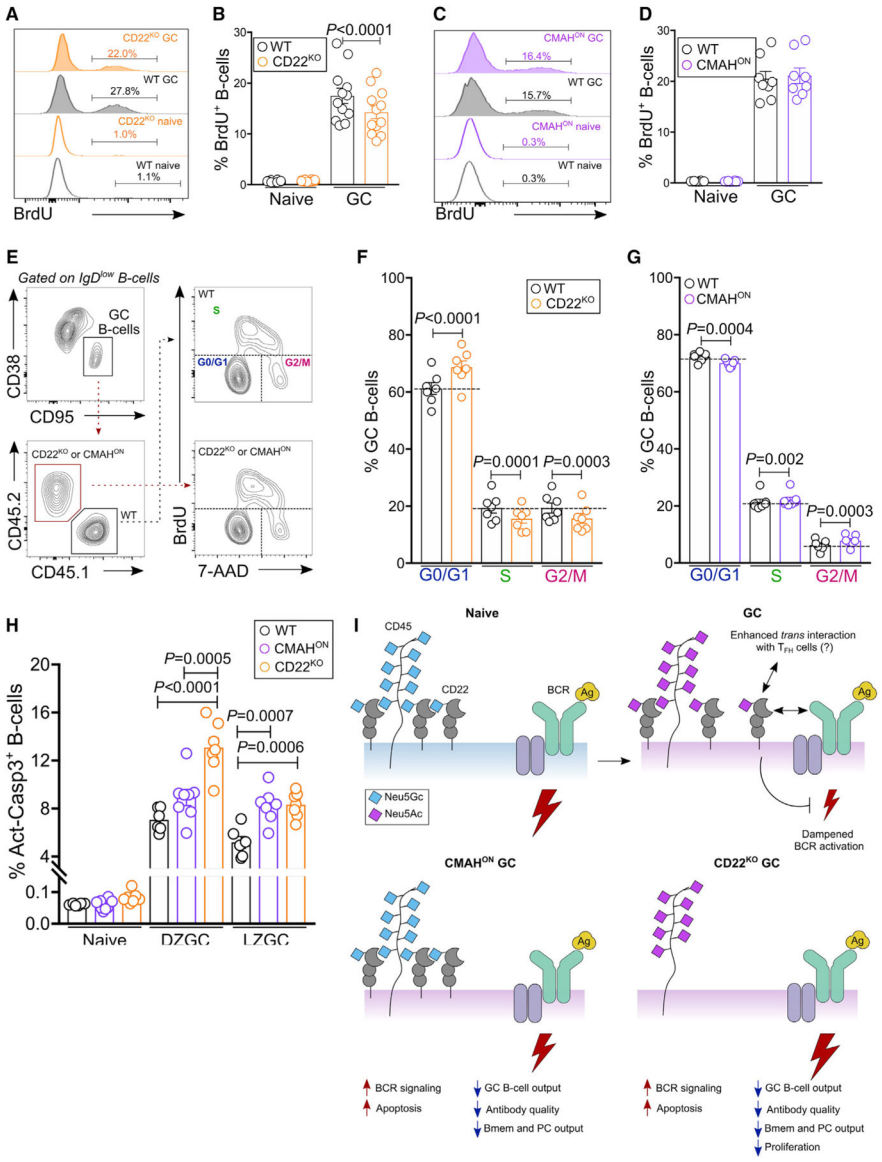

Figure 7. CD22^{KO} GC B cells display poor proliferation and cell cycle phase progression, as well as increased apoptotic cell death

(A and B) Representative flow cytometric histograms of BrdU^{+} cells in WT and CD22^{KO} naive and GC B cells (A) and quantification of percentage BrdU^{+} cells in WT and CD22^{KO} B cells (B). Pooled data from 2 independent experiments; n = 12 mice.

(C and D) Representative flow cytometric histograms of BrdU^{+} cells in WT and CMAH^{ON} naive and GC B cells (C) and quantification of BrdU^{+} cells in WT and CMAH^{ON} B cells (D). Pooled data from 2 independent experiments; n = 8 mice.

(E) Gating strategy for the flow cytometry-based analysis of cell-cycle phase progression.

(F and G) Quantification of WT and CD22^{KO} GC B cells (F) and WT CMAH^{ON} GC B cells (G) in different cell cycle phases. n = 6 or 7 mice/group.

(H) Quantification of percentage apoptotic naive, DZ GC, and LZ GC B cells from WT, CD22^{KO}, and CMAH^{ON} mice, at day 14 PI. n = 6–8 mice/group.

(I) Model for glycan remodeling on GC B cells. In naive B cells (upper left), CD22 forms nanoclusters with CD45 that sequester CD22 away from the BCR. Downregulation of the CMAH in the GC (upper right) results in a switch from Neu5Gc to Neu5Ac, leading to downregulation of CD22 ligands. This glycan remodeling is predicted to increase CD22-BCR association and enhance *trans* interaction with glycan ligands on $CD4^+$ T_{FH} cells. Constitutive CMAH expression (lower left) or CD22 deficiency (lower right) in GC B cells does not enable CD22 to negatively regulate the BCR, leading to a defective GC response. Data plots are presented as mean ± SEM. Statistical analysis was performed using paired Student's t test (B, D, F, and G), and Dunnett's multiple-comparison post one-way ANOVA (H).

KEY RESOURCES TABLE

REAGENT or RESOURCE	SOURCE	IDENTIFIER
Antibodies		
Rat anti-mouse B220 (clone:RA3–6B2)	BD Biosciences	cat# 563793; RRID: AB_2738427
Rat anti-mouse CD19 (clone: 6D5)	BioLegend	cat# 115555; RRID: AB_2565970
Rat anti-mouse CD38 (clone: 90)	BioLegend	cat# 102732; RRID: AB_2734153), 102716; RRID: AB_2073334, 102722; RRID: AB_2563333
Hamster anti-mouse CD19 (clone: Jo2)	BD Biosciences	cat# 563646; RRID: AB_2738345
Rat anti-mouse IgD (clone: 11–26c.2a)	BD Biosciences	cat# 563618; RRID: AB_2738322
Rat anti-mouse IgD (clone: 11–26c.2a)	BioLegend	cat# 405718; RRID: AB_10730619
Rat anti-mouse CD86 (clone: GL1)	BD Biosciences	cat# 560582; RRID: AB_1727518
Rat anti-mouse/human GL7 antigen (clone: GL7)	BioLegend	cat# 144606; RRID: AB_2562185, 144610; RRID: AB_2562979, 144620; RRID: AB_2800677
Rat anti-mouse CD184 (CXCR4) (clone: L276F12)	BioLegend	cat# 146506; RRID: AB_2562783, 146511; RRID: AB_2562788, 146517; RRID: AB_2687244
Mouse anti-mouse CD45.1 (clone: A20)	BioLegend	cat# 110738; RRID: AB_2562565, 110736; RRID: AB_2562564, 110718; RRID: AB_492862
Mouse anti-mouse CD45.2 (clone: 104)	BioLegend	cat# 109816; RRID: AB_492868, 109832; RRID: AB_2565511, 109841; RRID: AB_2563485, 109836; RRID: AB_2563065
Rat anti-mouse I-A/I-E (clone: M5/114.15.2)	BioLegend	cat# 107639; RRID: AB_2565894
Mouse anti-BrdU (clone: 3D4)	BioLegend	cat# 364108; RRID: AB_2566452
Rat anti-mouse CD138 (clone: 281–2)	BD Biosciences	cat# 561070 (RRID: AB_395000), 563147 (RRID: AB_2721029)
Rat anti-mouse CD22 (clone: OX-97)	BioLegend	cat# 126112; RRID: AB_2561632, 126108; RRID: AB_2074573, 126106; RRID: AB_2244414
Mouse anti-mouse CD22.2 (clone: Cy34.1)	BD Biosciences	cat# 740682; RRID: AB_2740369
Goat anti-mouse IgG1-HRP	SouthernBiotech	cat# 1071–05; RRID: AB_2794426
Goat F(ab')$_2$ anti-mouse Kappa UNLB	SouthernBiotech	cat# 1052–01; RRID: AB_2794386
Goat F(ab')$_2$ anti-mouse Kappa Biotin	SouthernBiotech	cat# 1052–08; RRID: AB_2819120
Rat anti-mouse CD21/CD35 (clone: 7G6)	BD Biosciences	cat# 553817; RRID AB_395069
Mouse anti-rat IgG2b (clone: MRG2b-85)	BioLegend	cat# 408209; RRID: AB_2715885
Mouse anti-mouse CD45.1 (clone: A20)	BioLegend	cat# 110738; RRID: AB_2562565, 110736; RRID: AB_2562564, 110718; RRID: AB_492862
Mouse anti-rat IgG2a (clone: 2A8F4)	SouthernBiotech	cat# 3065–30; RRID: AB_2795877
Chicken anti-Neu5Gc	BioLegend	cat# 146903; RRID: AB_2562884
Goat anti-chicken IgY secondary antibody	Invitrogen	cat# A21447; RRID AB_2535864
TruStain FcX™ PLUS (anti-mouse CD16/32) Antibody (clone: S17011E)	BioLegend	cat# 156604; RRID: AB_2783138
Mouse anti-mouse Nur77 (clone:12.14)	Invitrogen	cat# 12–5965-80; RRID AB_1257210
Donkey anti-rabbit IgG (clone: poly4064)	BioLegend	cat# 406421; RRID AB_2563484

REAGENT or RESOURCE	SOURCE	IDENTIFIER
Rabbit anti-cMyc (clone: D84C12)	Cell Signaling Technology	cat# 5605S; RRID: AB_1903938
Rabbit anti-phospho ribosomal protein S6 (S235/236) (clone: D57.2.2E)	Cell Signaling Technology	cat# 4858S; RRID: AB_916156
Rabbit anti-phospho Akt S473 (clone: D9E)	Cell Signaling Technology	cat# 4060S; RRID: AB_2315049
Rabbit anti-phospho Akt T308 (clone: D25E6)	Cell Signaling Technology	cat# 13038S; RRID: AB_2629447
Rabbit anti-phospho Zap-70 (Y319)/Syk (Y352) (clone: 65E4)	Cell Signaling Technology	cat# 2717S; RRID: AB_2218658
Chemicals, peptides, and recombinant proteins		
FITC-Peanut Agglutinin (PNA)	Vector Laboratories	cat# FL-1071
Biotin-PNA	Vector Laboratories	cat# B-1075
AF647-Chicken ovalbumin (OVA)	Invitrogen	cat# O34784
Purified Streptavidin	BioLegend	cat# 280302
AF488-Streptavidin	BioLegend	cat# 405235
Brilliant violet 605-streptavidin	BioLegend	cat# 405229
Brilliant violet 650-streptavidin	BioLegend	cat# 405232
Propidium iodide	Invitrogen	cat# P1304MP
7-AAD	BioLegend	cat# 420403
OVA	Sigma	cat# A-5503
NP_{23}-BSA	LGC Biosearch	cat# N-5050H
NP_2-BSA	Prepared in the lab	N/A
NP_4-APC	Prepared in the lab	N/A
NP_{20}-APC	Prepared in the lab	N/A
NP-OVA	Prepared in the lab	N/A
NP-OSu	LGC Biosearch	cat# N-1010–100
Tamoxifen	Combi-Blocks	cat# QC-0156
1,2-distearoyl-sn-glycero-3-phosphocholine (DSPC)	Avanti Polar Lipids	cat# 850365P
1,2-distearoyl-sn-glycero-3-phosphoethanolamine-N-[methoxy(polyethylene glycol)-2000] (ammonium salt) (PEG_{2000}-DSPE)	Avanti Polar Lipids	cat# 880120
Cholesterol	Sigma	cat# C8667
4% paraformaldehyde	Thermo Scientific	cat# J19943-K2
Polyethylenimine, branched	Sigma	cat# 408727
Lysozyme, chicken egg white (HEL)	Sigma	cat# 62971
N-succinimidyl 3-(2-pyridyldithio)-propionate (SPDP)	Thermo Scientific	cat# 21857
Maleimide-PEG_{2000}-DSPE	Avanti Polar Lipids	cat# 880126
Peroxidase substrate solution A	SeraCare	cat# 50–76-02
Peroxidase substrate solution B	SeraCare	cat# 50–65-02
Sepharose CL-4B	GE Healthcare	cat# 17–0150-01
Mouse IL4	BioLegend	cat# 574304
Mouse IL21	BioLegend	cat# 574504
5′-Atto647N-TCCGGCTGCCTCGCTGCCGTCGCCA-3′-biotin	IDT DNA	NA

REAGENT or RESOURCE	SOURCE	IDENTIFIER
5′-TGGCGACGGCAGCGAGGCAGCCGGA-3′	IDT DNA	NA
5′-TGGCGACGGCAGCGAGGCAGCCGGA-3′′-Iowa Black RQ	IDT DNA	NA
Critical commercial assays		
Mouse B-cell isolation kit	Miltenyi	cat# 130–090-862
LD columns	Miltenyi	cat# 130–042-901
CytoFix/CytoPerm buffer	BD Biosciences	cat# 554714
CytoPerm buffer plus	BD Biosciences	cat# 51–2356KC
True-Nuclear™ Transcription Factor buffer set	BioLegend	cat#424401
HiTrap Protein G HP column	GE Healthcare	cat# 17–0404-01
CountBright™ absolute counting beads	Invitrogen	cat# 36950
Fiji	ImageJ	https://imagej.net/Fiji
FlowJo v9	FlowJo	https://www.flowjo.com
GraphPad Prism v7	GraphPad Software	https://www.graphpad.com/scientific-software/prism/
ZEN blue	Zeiss	https://www.zeiss.com/
Galaxy platform (RNAseq analysis)	Galaxy	https://usegalaxy.org/